The photoinduced phase transitions of vanadium dioxide

Kunal Tiwari

Department of Physics
McGill University
Montréal, Québec, Canada
August 2014

A thesis submitted to McGill University
in partial fulfillment of the requirements of the degree of
Master of Science

© Kunal Tiwari

Abstract

The insulator-to-metal transition of vanadium dioxide has attracted the interest of condensed matter physicists for over half a century. In its high-temperature phase, VO_2 is metallic with tetragonal rutile crystallography. In its low-temperature phase, it has correlated semiconducting electronic character and a charge-density-wave-like paired monoclinic lattice structure. Determining the relative roles of electron-electron and electron-phonon interactions in the electronic structure of the low temperature phase has been the source of the physics community's interest in VO_2.

Over the past two decades, it has been shown that the insulator to metal transition may be photoinduced with ultrafast laser pulses. In this thesis we present ultrafast electron diffraction and ultrafast time resolved terahertz spectroscopy measurements of this photoinduced phase transition. Our ultrafast electron diffraction results reveal, at low fluences, a novel metastable phase. This phase has the crystallography of the insulating state, but a dramatically collapsed band gap. A reorganization of valence charge density accompanies this modulated spectroscopic activity.

These results have twofold significance. They show that the insulating behavior of the low temperature phase is affected primarily by electron-electron correlations, not by lattice structure. Importantly, they also show that ultrafast electron diffraction may be used to probe both electronic and lattice structure dynamics—it is sensitive to valence charge density reorganizations.

Our time resolved terahertz spectroscopy results complement these ultrafast electron diffraction data. We show that, in the novel metastable monoclinic phase, the band gap does not collapse below 50 meV. We also show that dynamics in the

time resolved terahertz conductivity through the full photoinduced phase transition occur on two timescales—one fast (240 femtosecond) timescale, characteristic of the coherent athermal photoinduced phase transition; and one slow (picosecond) timescale, characteristic of the astructural transition to the metastable monoclinic phase. In conjunction with our ultrafast electron diffraction measurements, these results suggest that the slow dynamics of the astructural phase transition, and the structural phase transition may be affected by the same underlying mechanism.

Résumé

Depuis plus d'un demi siècle, la transition de la phase métallique vers la phase isolante du dioxyde de Vanadium a captivé les physiciens du solide. Dans sa phase haute température, VO_2 est métallique, avec une structure cristalline tetragonale rutile. Dans sa phase basse température, le matériau possède des propriétés eléctroniques de semi-conducteur correlé ainsi qu'une structure de réseau monoclinique similaire à une onde de densité de charge.

La détermination de l'influence des intéractions électrons-électrons et électrons-phonons sur la structure électronique de la phase à basse température est à l'orignine de l'inérêt de la communauté pour ce matériau.

Au cours des deux dernières décennies, il a été montré que la transition de l'état isolant à métallique peut être photoinduite par un pulse laser ultrarapide. Dans la présente thèse, des mesures spectroscopiques de diffraction d'électrons ultrarapide ainsi que des mesures de conductivité transiente ultrarapide sont présentées.

Les résultats de diffraction d'électrons ultrarapide révèlent, pour des fluences faibles, une phase métastable jusqu'à lors inconnue présentant des propriétés crystallographiques d'une phase isolante, mais avec une largeur de bande dramatiquement réduite et une réorganisation de la densité de charge de valence. Ces résultats sont significatifs pour deux raisons. Ils démontrent que le comportement isolant de la phase basse température est principalement affecté par les corrélations électrons-électrons et non pas par la structure du réseau. Par ailleurs, les résultats démontrent également que la diffraction ultrarapide d'électrons est un moyen puissant d'étude de la dynamique structurelle des électrons et du réseau. La technique est ainsi capable d'observer la réorganisation de la densité de charge de valence.

Nos données résolues en temps dans le domaine spectral du Terahertz complémentent les résulats de diffraction ultrarapide. De manière définitive, nous montrons que, dans la nouvelle phase métastable monoclinique, la largeur de bande ne se réduit pas de plus de 50meV. Nous observons également que la dynamique de la conductivité Terahertz exhibe deux constantes de temps sur la durée complète de la transition de phase photoinduite: une première rapide (240 femtosecondes), charactéristique de la transition photoinduite cohérente athermique; et une plus lente (picoseconde), charactéristique de la transition astructurelle de la phase métastable monoclinique. Combinés avec nos mesures de diffraction d'électrons ultrarapide, nos résultats suggèrent que la dynamique lente de la transition de phase astructurelle et que la transition de phase structurelle pourraient être affectées par le même méchanisme sous-jacent.

Acknowledgements

I thank my supervisor, Prof. Bradley Siwck, for his enthusiastic support and guidance related to this project and science at large. The treatment of the results presented in this thesis would not have been fully realized without his creativity and breadth of knowledge. I would like to thank the whole Siwick group for their friendship and for the help they've given me as a scientist. I recognize Dr. Morrison in particular, whose work and expertise with vanadium dioxide made my project possible.

I would also like to thank Prof. David Cooke for his supervision related to the results presented in Chapter 5. Prof. Cooke graciously allowed me the use of his time resolved terahertz spectrometer for an extended period of time, and guided me through the maze of terahertz data analysis. I am similarly grateful for the help of David Valverde, who helped me run these experiments.

I thank Dr. Mohamed Chaker and Dr. Ali Hendaoui for preparing the VO_2 samples used throughout this thesis.

Finally, I am grateful my family's support and unconditional love throughout my life.

Table of Contents

Abstract ii

Résumé iv

Acknowledgements vi

List of Figures ix

1 Introduction 1

2 Methods 4

2.1 Pump-probe measurement 4
2.2 Ultrafast electron diffraction 5
2.2.1 Pulse generation 8
2.2.2 Radio frequency pulse compression 10
2.2.3 Detection 12
2.3 Terahertz spectroscopy 13
2.3.1 Time resolved terahertz spectroscopy 14
2.3.2 Terahertz pulse generation and detection 15
2.3.3 Pump, reference, and conductivity reconstruction 16

3 Vanadium dioxide prior art 18

3.1 Historical picture of VO_2 18
3.1.1 Goodenough 20
3.1.2 Mott 20
3.2 Contemporatary picture of VO_2 22
3.2.1 Modern theoretical and numerical treatments of VO_2 . . . 23
3.2.2 Contemporary experimental studies of VO_2 26
3.3 Chapter summary 39

4 Ultrafast electron diffraction of vanadium dioxide 41

4.1 Experimental 42
4.1.1 Samples 42
4.1.2 Experimental parameter space 42
4.1.3 Infrared transmissivity 42
4.2 Results 44
4.2.1 Pair distribution function analysis 45
4.2.2 Heterogeneous response 46
4.3 Discussion 50
4.3.1 The photoinduced structural phase transition 50
4.3.2 The metastable monoclinic conductor 50
4.3.3 Conclusions 52

5 Time resolved terahertz spectroscopy of vanadium dioxide 53

5.1 Experiment 54
5.1.1 Samples 54
5.1.2 Time resolved terahertz spectroscopy setup 54
5.1.3 Experimental parameter space 55
5.1.4 Analysis 55
5.2 Results 59
5.2.1 Direct current conductivity 59
5.2.2 Spectroscopic signatures 60
5.2.3 Fluence dependence 60
5.3 Discussion 65
5.3.1 $\Phi < \Phi_S$ 65
5.3.2 $\Phi > \Phi_S$ 65
5.4 Summary 66

References 67

List of Figures

Figure		page
2–1	A schematic of the pump-probe approach	5
2–2	Temporal probe locality in pulsed diffraction measurements	6
2–3	Schematic of a semiclassical bright electron pulse	9
2–4	Coulomb repulsion mediated electron pulse expansion	11
2–5	Position momentum profile of free propagating electron pulses	12
2–6	Schematic of radio frequency pulse compression	13
2–7	Schematic of a time resolved terahertz spectroscopy apparatus	15
3–1	Structure of low and high temperature VO_2 and geometry of t_{2g} bands	19
3–2	Schematic density of states diagram of Goodenough's treatment of the semiconductor metal transition	21
3–3	Free energy of VO_2 as a function of pairing parameter in the Mott picture	22
3–4	Schematic of the roles of lattice and electronic instabilities in the VO_2 spectral function due to Biermann	24
3–5	Schematic of the roles of lattice and electronic instabilities in the VO_2 spectral function due to Weber	25
3–6	X-ray absorption spectra of equilibrium VO_2	32
3–7	Photoemission spectra of equilibrium VO_2	33
3–8	Electronic and structural phase fraction non-congruence across the equilibrium phase transition	33

3–9 Time resolved x-ray diffraction of the photoinduced phase transition . 34

3–10 Coherent vibration in VO_2's infrared properties through the photoinduced phase transition 35

3–11 Time resolved electron diffraction of the photoinduced phase transition 36

3–12 Basal temperature dependent photoinduced phase transition threshold probed by terahertz spectroscopy 37

3–13 Spectrally resolved multi terahertz spectroscopy of photoinduced response above and below the phase transition fluence threshold . 38

4–1 Equilibrium VO_2 film sample characterization 43

4–2 Equilibrium micrographs of the used polycrystalline VO_2 sample, and a characteristic electron diffraction pattern. 44

4–3 Photoinduced diffraction signatures of VO_2 47

4–4 Diffraction signature of the VO_2's astructural photoinduced phase transition 48

4–5 Differential pair distribution functions of the structural and astructural photoinduced phase transitions 49

5–1 Equilibrium characterization of VO_2 thin film sample, and sample schematic 56

5–2 Time resolved terahertz spectroscopy apparatus schematic 57

5–3 Terahertz probe pulse characterization 58

5–4 Time and frequency resolved photoinduced changes in VO_2's real conductivity for characteristic fluences 62

5–5 Time dependence of extrapolated direct current conductivity for a set of characteristic fluences 63

5–6 Fluence dependence of the magnitue of slow and fast dynamics in extrapolated direct current conductivity 64

CHAPTER 1

Introduction

Over the past decades, the hard condensed matter physics community has become increasingly interested in complex systems. In this context, a complex system is one in which a plurality of interactions are simultaneously active [1]. Such systems host a number of nearly degenerate ground states and have accordingly complex phase diagrams. Further, this degeneracy often leads to nanoscale inhomogeneity, emergent properties, and hysteretic behavior [1–3]. Examples of complex phenomena include colossal magnetoresistance, high-temperature superconductivity, and multiferroic behavior.

These systems are interesting because they are difficult to understand. Traditional theoretical methods are tuned to treat systems where a single interaction dominates. For example, in traditional Mott insulators, strong electron-electron interaction in a single band lead to an ordered state. This physics is well described by the simple Hubbard model. In traditional superconductivity the ground state may be understood in similar terms once the pairing mechanism is identified. In complex systems, no such simple description will suffice—it accounts neither for competition between interactions nor for the resultant inhomogenous phases.

Experimental characterization of complex systems is similarly challenging. Traditional diffraction and spectroscopy techniques probe spatially averaged sample volumes. Interpretation of these measurements, in terms of homogeneous models, is inherently flawed. Additionally, these measurements record only the net effect of competing interactions, not their individual contributions to the bulk. Methods that are able to characterize spatially inhomogeneous phases and methods that may parse the relative roles of competing instabilities will be essential to further our understanding of complex hard condensed matter systems.

The ultrafast sciences—able to measure the response of material properties to impulsive stimuli—represent a promising new probe of complex systems. By measuring the disparate time scales of response of different active degrees of freedom, ultrafast methods are able to infer their individual contributions to bulk properties. In this thesis, we present ultrafast electron diffraction and terahertz spectroscopy measurements on the transition metal oxide VO_2. VO_2 is an archetypal electronically complex material. Its infamous phase transition, at 340 K, includes a structural and an electronic reorganization from a semiconducting low temperature phase to a metallic high temperature phase [4]. For several decades, the condensed matter physics community has endeavored to understand the relative roles of electron-electron correlations and a Peierls type electron-phonon instability in determining the properties of the low temperature phase.

The results presented here have manyfold significance: they establish the ultrafast sciences as a powerful new tool of complex systems, specifically demonstrating that ultrafast electron diffraction may measure transient valence charge reorganizations; they identify a novel metastable phase of VO_2 with the structure of the low temperature phase but electronic properties between the two equilibrium phases;

and they suggest that there exist both thermal and athermal mechanisms of the photoinducable structural phase transition.

This thesis is divided into two chapters of background material and two chapters of experimental results. In Chapter 2 we summarize the experimental methods relevant to this study. In Chapter 3 we review the experimental and theoretical history of the study of VO_2. In Chapter 4 we present ultrafast electron diffraction data on the photoinduced phase transitions of VO_2. In Chapter 5 we present time resolved terahertz spectroscopy measurements in a fluence regime complementary to the time resolved diffraction work.

CHAPTER 2

Methods

The two experimental methods used in subsequent chapters, ultrafast electron diffraction and terahertz spectroscopy, fall under the umbrella of the ultrafast sciences. The goal of such methods is to infer otherwise hidden properties of materials based on their response to a stimuli [5]. A brief explanation of the novel perspective this emerging field provides to the study of material properties is given before a more detailed treatment of time resolved diffraction and time resolved terahertz spectroscopy.

2.1 Pump-probe measurement

The ultrafast techniques used in this thesis examples of pump-probe methods a schematic of which is given in Fig. 2–1. A pump pulse stimulates a response in a sample. After a fixed time delay, τ_{P-p}, the state of the responding sample is measured by a probe pulse. By taking data for a number of pump-probe delays, one may infer the sample's stimulated dynamics [6].

These time domain approaches have femtosecond resolution—shorter than most relevant process in condensed matter physics. Because of this, one may use ultrafast

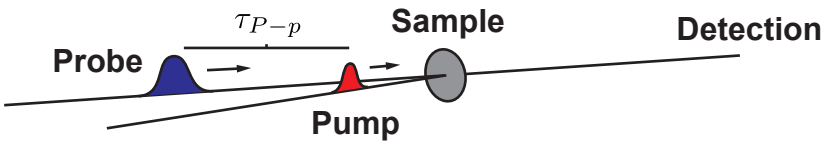

Figure 2–1: A schematic of the pump-probe approach. A pump pulse (red) stimulates a response of the sample. After a fixed time delay, τ_{P-p}, a probe pulse interrogates the state of the sample. By scanning τ_{P-p} one may extract the average dynamical response of the sample to the pump pulse.

methods to directly watch how specific impulsive excitations couple through a system's degrees of freedom. Ultrafast methods may measure natural timescales of these processes and accordingly have the potential to separate complex phenomena into their component pieces. For example, given the ability to measure lattice vibrations in a material affected in a material following the electronic excitation of a particular mode, one may directly measure the electron phonon coupling tensor. Alternatively, by measuring the spectroscopy of a material after perturbation, one may understand how its electronic structure is modified by the perturbation [7]. Strong impulses may also be used to drive systems far from equilibrium. In this regime, systems may be driven through phase transitions, and to metastable states [8].

2.2 Ultrafast electron diffraction

Ultrafast electron diffraction measures transient changes in the spatial configuration of a sample's potential, A_0. The aim of the technique is to acquire a high-quality, time-resolved diffraction pattern by interacting a bright, brief pulse of electrons with a sample.

In a traditional transmission electron microscope, a field emitting cathode is used to produce a steady state beam of individual electrons with well defined energy. Each of these electrons scatter off of (A_0), interfering with themselves before being detected

at far field. The ensemble measurement of these electrons' final positions produces a diffraction pattern characteristic of the sample's potential. Since the diffracted beam is steady-state, the pattern recorded is time averaged. As a consequence, dynamics within the sample cannot be measured by traditional transmission electron microscopy techniques.

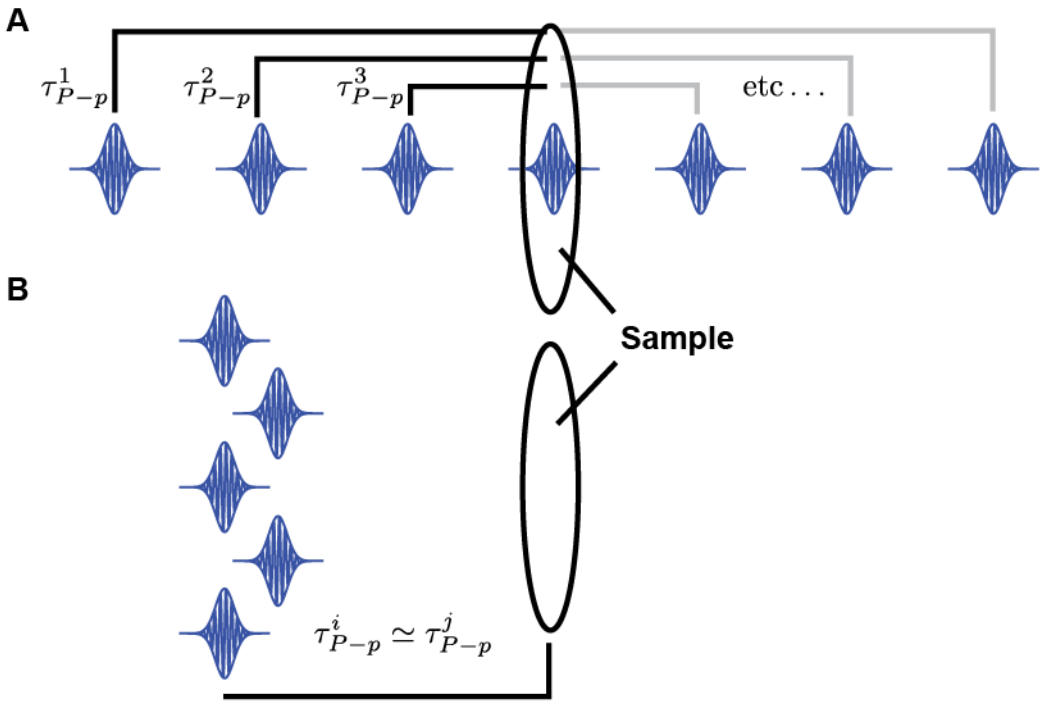

Figure 2–2: The contrasting modes of diffraction in transmission electron microscopy and ultrafast electron diffraction. A) in transmission electron microscopy, electrons are diffracted through the sample in series, forbidding the definition of a consistent τ_{P-p}. B) by diffracting a large number of electrons through a sample in parallel, ultrafast electron diffraction circumvents this shortcoming. This temporally local probe allows ultrafast electron diffraction to sample dynamical processes in A_0.

In an ultrafast electron diffraction experiment, the steady state electron beam is replaced by a brief, bright pulse of many electrons. Thus, in contrast to traditional transmission electron microscopy, the measurements made by ultrafast electron diffraction are well defined in time (Fig. 2–2). Naturally, one may anticipate the probe pulse with an impulsive perturbation. From a set of patterns for an appropriate range of τ_{P-p} they may then infer impulsively stimulated changes in the sample's potential. Practically, this means that ultrafast electron diffraction probes the impulse response in lattice degrees of freedom–the periodicity of which dominates the form of the potential. The mathematical description of this process is well established [9], and is summarized subsequently.

An electron incident on the sample has initial state

$$\psi\left(\mathbf{r'}\right) \simeq e^{i\mathbf{k_0}\cdot\mathbf{r'}}. \tag{2.1}$$

The time dependence of the wave is inconsequential to the subsequent derivation, and $\mathbf{k_0}$ is determined by the electron's energy. The electron interacts with the ∼classical electrostatic potential of the sample through

$$e\bar{\psi}\psi A_0. \tag{2.2}$$

For small angles, and elastic scattering this process is isotropic. Therefore, we can take the amplitude that an electron scatters to a new state, $\mathbf{k}$, to be determined completely by ψ, A_0, and the interaction strength e. The total scattered state at far field is determined by the superposition of these amplitudes from throughout the

sample.

$$\psi(\mathbf{r}) \propto \int_{\text{Sample}} A_0(\mathbf{r}')\, e^{i\mathbf{k_0}\cdot\mathbf{r}'} e^{i\mathbf{k}\cdot(\mathbf{r}-\mathbf{r}')} \mathrm{d}^3\mathbf{r}' \tag{2.3}$$

$$= e^{i\mathbf{k}\cdot\mathbf{r}} \mathcal{F}\left[A_0(\mathbf{r})\right]. \tag{2.4}$$

This transform is defined in the literature as ($\mathbf{\Delta k} = \mathbf{k_0} - \mathbf{k}$)

$$f(\mathbf{\Delta k}) = -\frac{m_e}{2\pi\hbar^2} \int_{\mathbb{R}^3} A_0(\mathbf{r}')\, e^{-i\mathbf{\Delta k}\cdot\mathbf{r}'} \mathrm{d}^3\mathbf{r}'. \tag{2.5}$$

A diffractometer measures $|\psi(\mathbf{\Delta k})|^2$, the probability that an electron is scattered with $\mathbf{\Delta k}$. As we have shown, this probability is determined by the periodicity of A_0. In a time resolved diffraction experiment, dynamics in A_0 are affected by a pump pulse. The aim of ultrafast electron diffraction is therefore to measure $A_0(\tau_{P-p})$. Implicit above is the assumption that given the pump stimulated dynamics, the electron scattering process is still dominated by A_0, as in Eq. 2.2.

Producing a well defined τ_{P-p} is slightly complicated by the electron–electron scattering interaction. The following subsections discuss the practical challenges associated with time resolved diffraction experiments: electron pulse generation, electron pulse compression, and electron pulse detection.

2.2.1 Pulse generation

Given the existence of femtosecond laser systems, the generation of sub-picosecond electron pulses is simple. By illuminating a metal at or above its work function, an ultrashort cloud of photoemitted electrons is produced. An accelerating voltage is then used to boost the pulse towards a sample.

The diffractometer used in Chapter 4 works on precisely this principle. A copper cathode is illuminated with a bright 35 femtosecond pulse of ultraviolet (4.6 eV)

light. The cathode is kept near 100 kV from the grounded anode. The photoemitted electron pulse is accelerated by this potential down the a beam line towards the sample.

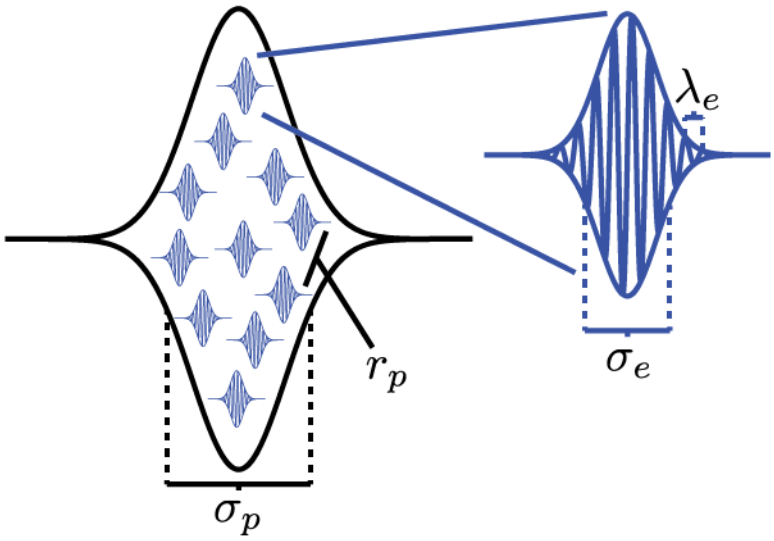

Figure 2–3: Schematic of a semiclassical bright electron pulse. The mean inter-electron distance substantially exceeds the mean individual electron envelope. Within the single electron envelope, each electron has a well defined wavelength.

In the regime relevant to the present experiments, it is appropriate to think of the generated electron pulse semi-classically as a cloud of particles characterized by (a) an intrinsic particle carrier wavelengthm λ_e, (b) an individual particle envelope, σ_e, and (c) a inter particle radius, r_p. This view is summarized in Fig. 2–3. The wavelength of the pulse's electrons is determined by

$$\lambda_e = \frac{h}{\sqrt{\frac{e^2U^2}{c^2} + 2eUm_e}} \tag{2.6}$$

and the electrons travel at

$$v_e = \frac{1}{\gamma}\sqrt{\frac{e^2U^2}{m_e^2c^2} + \frac{2eU}{m_e}}. \tag{2.7}$$

The wave packet envelope, σ_e is determined by the generating femtosecond pulse, the properties of the cathode, and the vacuum dispersion. Finally, the inter particle radius r_p is determined primarily by inter electron repulsion. This final parameter is, in the relevant regime, equivalent to the total pulse length, σ_p, which ultimately determines the time resolution of the experiment.

For $r_p \gg \sigma_e$, the individual electron wave packets are approximately orthogonal. Thus, we may construct the wave function of the entire pulse simply as antisymmetric linear combination these packets. Given the existence of this one-particle basis and the conditions that $\sigma_e \gg \lambda_e$, the applicability of the preceding monochromatic diffraction analysis is clear.

2.2.2 Radio frequency pulse compression

While producing a femtosecond electron pulse is a rather easy enterprise, maintaining this short pulse duration is more challenging. Electrons within the a pulse naturally repel each other—those at the pulse front are accelerated by the lagging net charge, and those at the back are retarded. Siwick [10] treats this process in some detail. A heuristic description of this process, and the solution implemented by Morrison and Chatelain [11] is given here.

Pulse broadening depends on many parameters, including the number of electrons in the pulse, the transverse pulse width, and the initial pulse duration. Compact pulses are essential for ultrafast electron diffraction experiments, at odds with the effect of each of these expansion parameters. The simulated expansion of archetypal pulses are given in Fig. 2–4. Pulses of $\mathcal{O}\{10^6\}$ electrons, two orders of magnitude

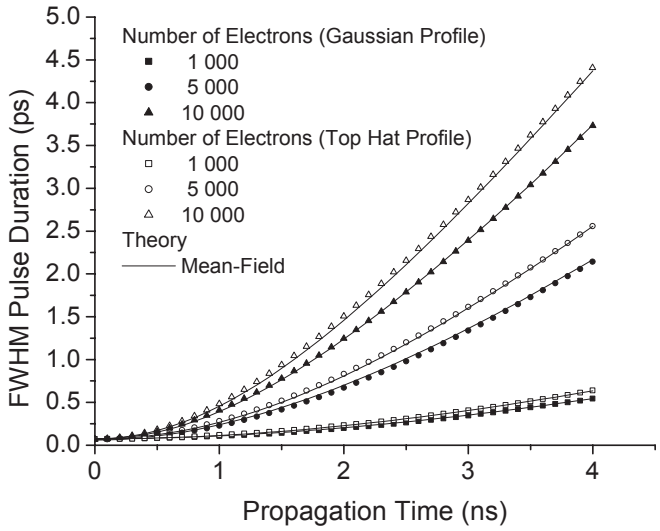

Figure 2–4: The FWHM of the electron packets kinetic energy distribution vs. propagation time, and its dependence on N for a top-hat transverse profile beam (N = 1000, 5000 and 10000, τ_o = 90 fs, $r(0) = 250\mu$m). The electron pulse generates many eV of kinetic energy bandwidth as it propagates due to space-charge effects. Figure 3 of Siwick *et al.*, *"Ultrafast electron optics: Propagation dynamics of femtosecond electron packets" [10]*

higher than those in Fig. 2–4, are needed to efficiently acquire data with sufficient signal to noise. Expansion effects in such bright pulses quickly lead to prohibitively large σ_P.

As a pulse propagates and expands, it develops a linear position-momentum relationship (chirp). This process is shown in the phase space diagrams of Fig. 2–5. Because of this position momentum-relationship, radio frequency pulse compression may be used to counteract the electron pulse's natural expansion [12]. By applying time varying longitudinal electric field with the propagation of the electron pulse, one may invert its linear chirp. The electron pulse collapses to its initial configuration a fixed time later, affecting the desired short pulse duration. This approach is illustrated in Fig. 2–6.

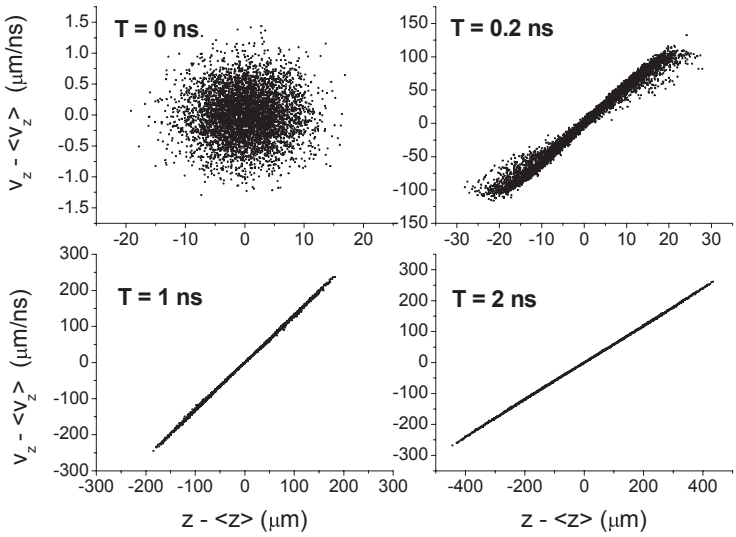

Figure 2–5: Relative axial velocity vs. axial position for all electrons in the pulse at four times, T, during its propagation ($N = 10\ 000$, $\tau_o = 150$ fs, $r(0) = 75$ μm, 1.5 mrad initial beam divergence). The width of the velocity distribution becomes larger as the ouse lengthens. The spatial distribution of the velocities also evolves. As electrons redistribute themselves inside the packet a linear velocity chirp develops on the electron pulse. Figure 6 of [10]

Morrison and Chatelain implemented this approach in the diffractometer used to obtain the results presented in Chapter 4. σ_p for this apparatus was measured at the sample position to be 140±4 fs. Details of the implementation and characterization of the device may be found in the instrument paper [11] and the authors' theses [13,14].

2.2.3 Detection

The same technology developed for traditional transmission electron microscopy may be used to measure the scattered electrons post-specimen. A phosphorescent plate coupled to a CCD records the transverse coordinates of incoming electrons for a given τ_{P-p}.

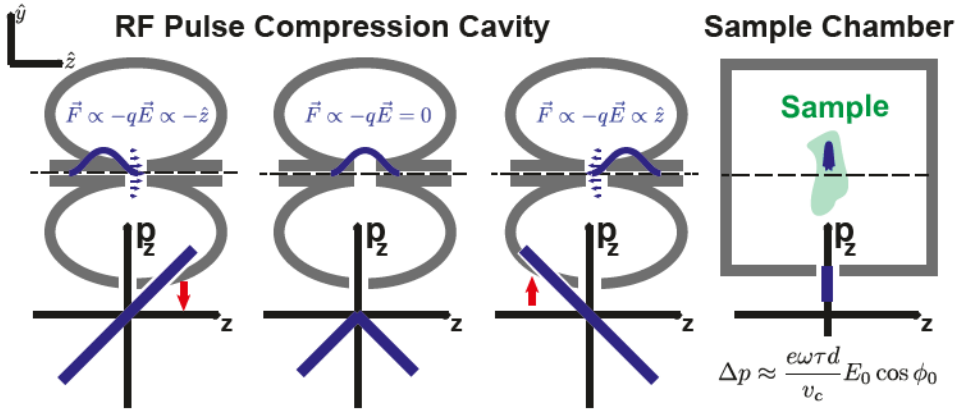

Figure 2–6: Schematic of the RF pulse compression technique. By properly timing an oscillating RF field, the high momentum electrons at the front of the pulse are retarded while the trailing slow electrons are accelerated. This momentum distribution inversion causes the pulse to collapse upon itself at the sample, yielding a short pulse duration.

2.3 Terahertz spectroscopy

The terahertz frequency range is host to an abundance of interesting processes [15]. In solids and molecules, many optically active phonon transitions fall in the THz regime. In metals, inverse mean free scattering times fall primarily in the THz domain. Further, excitonic and other bound charge states often have revealing THz signatures.

Terahertz spectroscopy aims to quantitatively characterize the electronic properties of materials in the terahertz regime. Like traditional ultraviolet, visible, and infrared spectroscopies, this is accomplished by the transmission or reflection of terahertz radiation through a sample of interest. Uniquely, one is able to easily record the total waveform of transmitted terahertz radiation. Given this additional phase information, one may reconstruct the total sample specific complex conductivity. This practical advantage, coupled with the abundance of ubiquitous interactions

in the meV range, makes terahertz spectroscopy a exceptionally powerful probe of electronic structure.

2.3.1 Time resolved terahertz spectroscopy

In a time resolved terahertz spectroscopy experiment, an impulsive pump pulse stimulates a sample response. A terahertz probe pulse is used to interrogate the pump-probe delay dependent changes in the sample's meV electronic structure. In turn, after transmission through the sample, the terahertz probe pulse is sampled by a third pulse. By scanning this sampling pulse against the terahertz pulse, one is able to record the complete terahertz waveform. In this way, time resolved terahertz spectroscopy is able to extract the complete complex conductivity (dielectric function) across the bandwidth of the probe.

The time resolved terahertz spectroscopy setup used in Chapter 5 is described in Fig. 2–7. A standard Ti:Sapphire (1.55 eV, 35 fs) system drives the apparatus. The primary beam is split into pump and probe lines. For fluence control, the pump line is modulated by a wave plate polarizer before being focused near the sample position. The probe line traverses a delay stage, governing τ_{P-p}, before being further split into a THz generating pulse and a sampling pulse for detection. By virtue of the τ_{P-p} delay stage, the probe pulse is always sampled τ_{P-p} relative to the pump arrival. The THz generating line passes another delay stage, which is used to scan the THz waveform relative to the triggered detector, before the THz generation medium. After THz generation, a silicon wafer is used a THz bandpass filter. The sample, THz source, and THz detector are all contained within a nitrogen environment—water has several active modes in the THz band.

Data is recorded for each pump-probe time delay both with and without the pump pulse. From these waveforms, the differential transmission coefficient may be

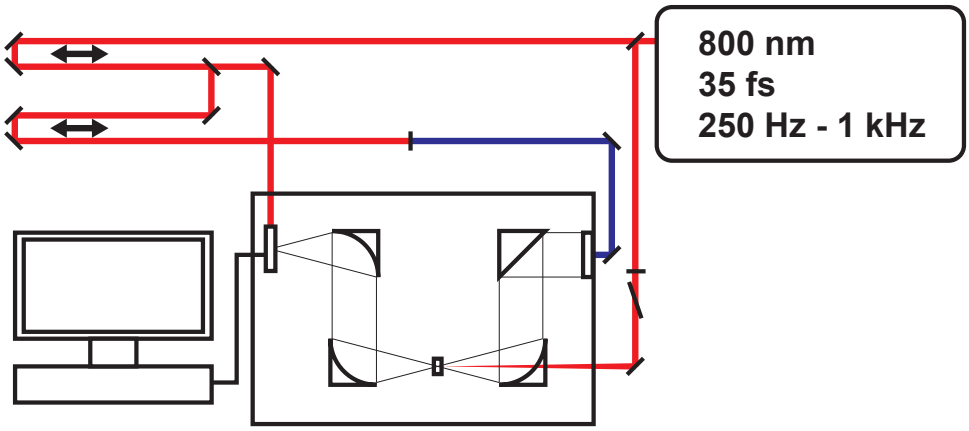

Figure 2–7: Schematic of a time resolved terahertz spectroscopy apparatus. A primary delay stage controls the relative arrival times of the pump and THz sampling pulses, while a secondary delay stage scans the generated terahertz pulse in this reference frame. The terahertz generation and detection are performed by nonlinear mixing processes in ionized plasma and air respectively.

determined. This property is uniquely determined by the intrinsic properties of the sample, and possibly the experimental geometry.

2.3.2 Terahertz pulse generation and detection

The terahertz spectrometer used for the present work is based upon an AC-bias plasma terahertz generation method. In this approach, an 800 nm pulse is focused with its temporally overlapped second harmonic. The resultant plasma's nonlinear polarization, driven by the product of the input field envelopes, acts as a THz radiation source. This process was proposed in [16] and an expanded explanation is given in [17]. Detection of the terahertz probe is possible through the reciprocal nonlinear mixing process. The particulars of detection are discussed in [18].

2.3.3 Pump, reference, and conductivity reconstruction

Because both terahertz generation and detection depend on nonlinear processes, they are exceedingly sensitive to power fluctuations. To measure a differential transmission coefficient independent of these fluctuation, one must record both the pumped and unpumped transmitted terahertz pulses for a given laboratory time. This is easily accomplished by placing a chopper in the pump line preceding the sample. Lockin amplifiers are used to record both the average transmitted field, E_{Abs}, for a particular $\{\tau_{P-p}, \tau_{THz}\}$, and the difference, E_{Diff}, affected by the chopper. Given these, one may easily reconstruct the transmitted probe for the pumped and the unpumped (reference) sample

$$E_{Pump}\left(\tau_{P-p}, \tau_{THz}\right) = E_{abs}\left(\tau_{P-p}, \tau_{THz}\right) + E_{diff}\left(\tau_{P-p}, \tau_{THz}\right) \tag{2.8}$$

$$E_{Ref}\left(\tau_{P-p}, \tau_{THz}\right) = E_{abs}\left(\tau_{P-p}, \tau_{THz}\right) - E_{diff}\left(\tau_{P-p}, \tau_{THz}\right). \tag{2.9}$$

The differential transmission coefficient is then simply

$$T\left(\tau_{P-p}, \omega\right) = \frac{E_{Pump}\left(\tau_{P-p}, \omega_p\right)}{E_{Ref}\left(\tau_{P-p}, \omega_p\right)} \tag{2.10}$$

with

$$\Delta\phi\left(\tau_{P-p}, \omega_p\right) = \arg\left[\Delta T\left(\tau_{P-p}, \omega_p\right)\right] \tag{2.11}$$

$$\left|\Delta T\left(\tau_{P-p}, \omega_p\right)\right| = \mathrm{abs}\left[\Delta T\left(\tau_{P-p}, \omega_p\right)\right] \tag{2.12}$$

Finally, in the case of a thin (relative to THz wavelengths) film sample, one may analytically extract the τ_{P-p} dependent complex conductivity from the transmission

coefficient [15, 19].

$$\sigma_1(\tau_{P-p}, \omega_p) = \frac{n_{sub}+1}{\Omega_{sub} \cdot d}\left(\frac{\cos\Delta\phi}{|\Delta T|} - 1\right) \tag{2.13}$$

$$\sigma_2(\tau_{P-p}, \omega_p) = \frac{n_{sub}+1}{\Omega_{sub} \cdot d}\left(\frac{\sin\Delta\phi}{|\Delta T|}\right). \tag{2.14}$$

Here, n_{sub} is the index of refraction of the semi infinite substrate on which the film is mounted (air), d is the thickness of the thin film, and Ω_{sub} is the impedance of the semi infinite substrate (again, air).

CHAPTER 3

Vanadium dioxide prior art

3.1 Historical picture of VO_2

The semiconductor to metal phase transition in VO_2 was first discovered in 1959 at Bell Laboratories [4]. In his seminal paper, Morin notes the unusual hysteresis of VO_2's conductivity around the transition temperature, $T_c \simeq 340$ K. As hysteresis is not usually found through the Neel temperature, this discovery suggested that an instability distinct from or more subtle than simple magnetic ordering affected the transition. Theoretical methods for strongly correlated electron systems were in their infancy at the time of the transition's discovery so VO_2 naturally became an archetypal material in this field.

In its low temperature phase, VO_2 has a monoclinic $P2_1/c$ structure [20]. In its high temperature phase, it has a rutile $P4_2/mnm$ structure. The crystal structures are given in Fig. 3–1. Roughly, the structural phase transition may be understood as a periodic lattice distortion in rutile c access accompanied by antiferroelectric distortion of the vanadium ion pairs.

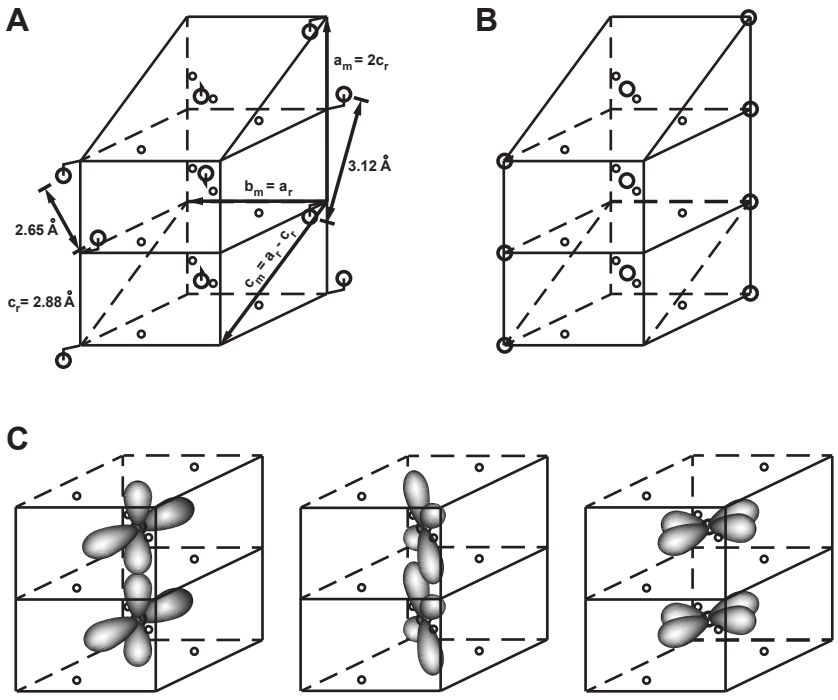

Figure 3–1: (A) the structure of monoclinic VO_2 over the doubled unit cell of the (B) rutile structure. Adapted from J. B. Goodenough, Journal of Solid State Chemistry **3**, 490 (1971). (C) from left to right the $d_{||}$, d_{xz}, and d_{yz} orbitals that compose bands near the Fermi surface. The small closed circles represent the oxygen ionic cores, while the large closed circles represent the vanadium ionic cores

The density of states of metallic rutile VO_2 is shown in on the left in Fig. 3–2, and is formed from the orbitals in Fig. 3–1 C. The broad d_{xz} and d_{yz} bands are hybridized with the nearby oxygen valence orbitals. In this phase, the $d_{||}$ and two other anti bonding d_{π^*} (d^*_{xz} and d^*_{yz}) all cross the Fermi surface. The two remaining d orbitals hybridize quite strongly with the oxygen valence orbitals—their respective anti-bonding bands are well above the Fermi surface [20].

The condensed matter physics community's interest in VO_2 stems from its insulating phase. The relevant bands (t_{2g}) near the Fermi surface are quite narrow. This suggests that their constituent orbitals have only small overlap, which, in turn, leads to a suppression of mean-field-like behavior. Thus it is natural to expect that strong electron correlations play an important role. Whether these correlations, or the structural distortions in the low temperature phase dictate the electronic properties is the fundamental question of interest.

3.1.1 Goodenough

Goodenough's treatment of VO_2

The first widely accepted theoretical treatment of VO_2 was published in 1971 by J. B. Goodenough [20]. In his paper, Goodenough argues that the symmetry of the underlying ionic lattice is responsible for the electronic phase transition through a simple band picture. The mechanism may be divided into two components. (a) the translation of vanadium anions orthogonal to the rutile c axis destabilizes the otherwise partially filled d_{π^*} (d_{xz} and d_{yz}) conduction bands above the Fermi energy. The electrons from these bands are displaced to the $d_{||}$. (b) the now half filled $d_{||}$ band is susceptible to a Peierls instability, which opens the gap about the Fermi energy. A density of states diagram of the proposed mechanism is given in Fig. 3–2. The arguments presented in Goodenough's paper are all based in the orbital overlaps affected by the crystal structure.

3.1.2 Mott

Mott's treatment of VO_2

Following Goodenough's proposal, an M_2 phase of VO_2 was discovered in the presence of doping [21–23]. These results suggested that Mott–Hubbard physics

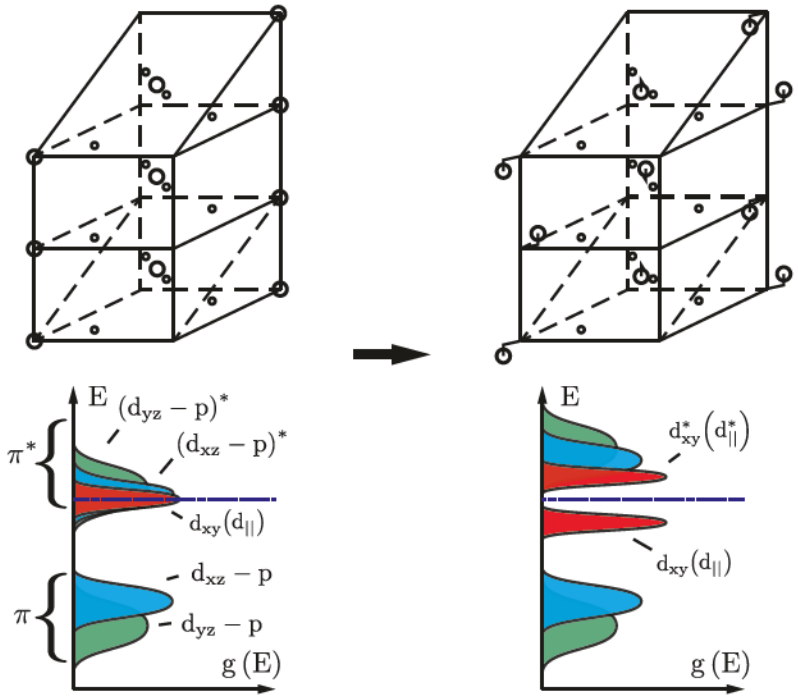

FIGURE 3–2: Schematic density of states diagram of Goodenough's treatment of the semiconductor metal transition.

plays an important role in the electronic phase transition. In response, Mott and Friedman published a competing theory of the transition [24]. Mott argued that the paired VO_2 atoms' molecular bonding electrons will necessarily interact through a Hubbard U with any valence electron to open a gap of

$$\Delta = U - \frac{1}{2}\left(B_{val} + B_{con}\right) + \Delta_{pair} \tag{3.1}$$

where the B's are the bandwidths (i.e. the widths of the $d_{x,y}$ in Fig. 3–2) and Δ_{pair} is the gap affected by the periodic lattice distortion (i.e. the separation of d_{xy} and d^*_{xy} in Fig. 3–2). Mott qualitatively sketches the free energy of the system as a function of ϵ, the magnitude of pairing displacement of the V atoms on the rutile axis. He concludes that there will be a temperature dependent local minimum in the

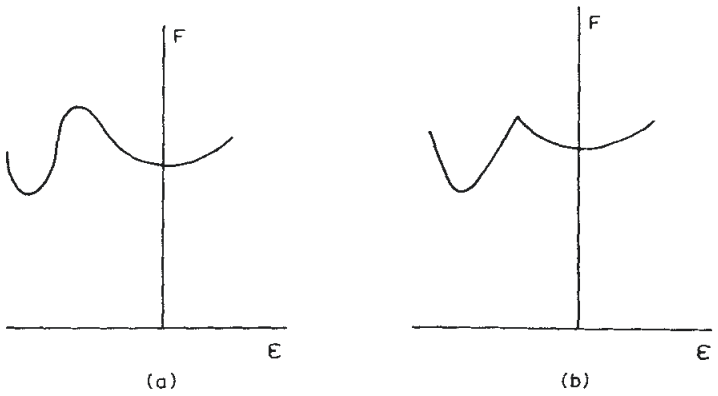

Figure 3–3: Possible curves of free energy at zero T against pairing parameter for VO_2. Figure 2 from N. F. Mott and L. Friedman, Philosophical Magazine **30**, 389 (1974).

system's free energy for a finite ϵ; for a low enough T this minimum is global, hence a the structural phase transition occurs (Fig. 3–3). The Hubbard U in this picture plays a determining role in the relative stability of the paired and unpaired states. Additionally, the magnitude of the gap is dominated by U.

3.2 Contemporatary picture of VO_2

The modern view of the phases of VO_2 is even more multifaceted. Sophisticated experimental techniques are able to provide exquisitely detailed data, and powerful numerical methods capture most properties of the low temperature phase. The caveat of these detailed data sets is that measured properties are often dependent on extrinsic sample properties such as microstructure. Similarly, the interpretation of modern numerical techniques is less well defined than that of the above mentioned analytical arguments. The fundamental goal of the study of VO_2 remains understanding the relative roles of electronic correlations and lattice structure in the determination of its phase diagram. In this section, I have attempted to elucidate the

results of the important modern works as they apply to this goal: I present the modern theoretical (numerical) perspective on VO_2, established by dynamical mean field theory; I highlight important equilibrium studies, both structural and electronic; and finally, I review the important time resolved studies of VO_2's photoinduced phase transitions.

3.2.1 Modern theoretical and numerical treatments of VO_2

Density functional theory

Following Mott's publication, the next notable advances in our understanding of VO_2 came with the advent of modern numerical techniques, namely density function theory (DFT). In the 1990s Renata Wentzcovitch *et al.* published a milestone DFT (LDA) treatment of VO_2. Significantly, Wentzcovitch *et al.* found a free energy minimum for a structure very similar to the M_1 phase [25–27]. However, their simulations failed to open a gap (by -0.04 eV). They note that LDA theory typically underestimates gap sizes and therefore conclude that the electronic phase transition is governed by physics within the LDA approximation. This work was significant in that it predicted the low temperature crystal structure from first principles, and in that it suggests that the latent heat of the transition is associated with the structural component. Wentzcovitch *et al.* did not address the insulating behavior of the M_2 phase, and did not explicitly predict the gap of the M_1 phase. Thus, the VO_2 transition remained unsolved.

Dynamical mean field theory

Dynamical mean field theory is the most wildly accepted numerical method for electronic structure calculations in correlated materials [28, 29]. It aims to capture the effects of dynamical correlations (e.g. the sampling of the nearest neighbor state

in a traditional Mott insulator) on the spectral function and orbital occupation of condensed matter systems. A good introductory review of dynamical mean field theory can be found in [28], while a more detailed treatment may be found in [29]. Two modern dynamical mean field theory studies of VO_2 compete as the accepted picture of VO_2's electronic structure—both conclude (albeit in different ways) that electronic correlations are a necessary component of the low temperature picture.

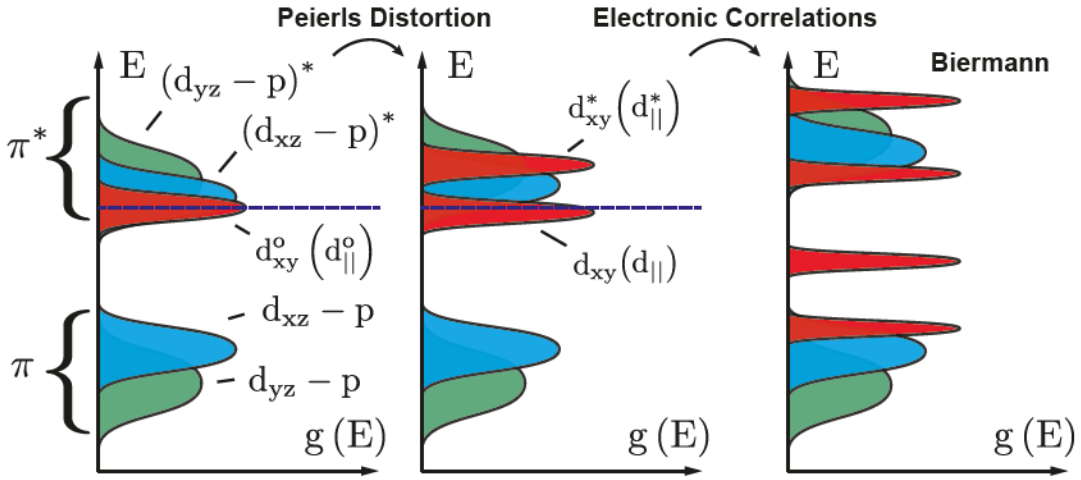

Figure 3–4: The relative effects of lattice distortion and electron-electron correlations on VO_2's spectral function as predicted by the dynamical mean field theory treatment of [30]. This figure is based on a personal communication with Cedric Weber.

Biermann *et al.* treat the three relevant t_{2g} orbitals (occupied by a total of one electron) within a cluster dynamical mean field theory framework [30]. Furthermore, they expand the cluster to include non-local self energy effects between codimerized vanadium orbitals. Numerical predictions based on these kinematics were given for both the R and the M_1 structure. For the R structure, Biermann *et al.* find a metallic phase with moderate bandwidth reduction affected by correlation effects. This phase has moderately increased occupation of the $d_{||}$ band (0.42) over the d_{yx}

and d_{xz} bands (each 0.29). For the M_1 structure, Biermann *et al.* find that the inclusion of the non-local intradimer self energy affects a gap in the spectral function of 0.6 eV. In this phase, the authors find significantly augmented occupation of the $d_{||}$ band (to 0.8) over the d_{yz} and d_{xz} (0.1). This orbital redistribution is directly linked to the intradimer nonlocal self energy, suggesting a singlet type ordered state among the two electrons of a given dimer. Biermann *et al.* note that their predicted state is not a conventional Mott insulator as there is not long range magnetic order. It should instead be viewed as a correlated state of dynamical singlets. A schematic of the spectral function implied by Biermann's picture is given in Fig. 3–4

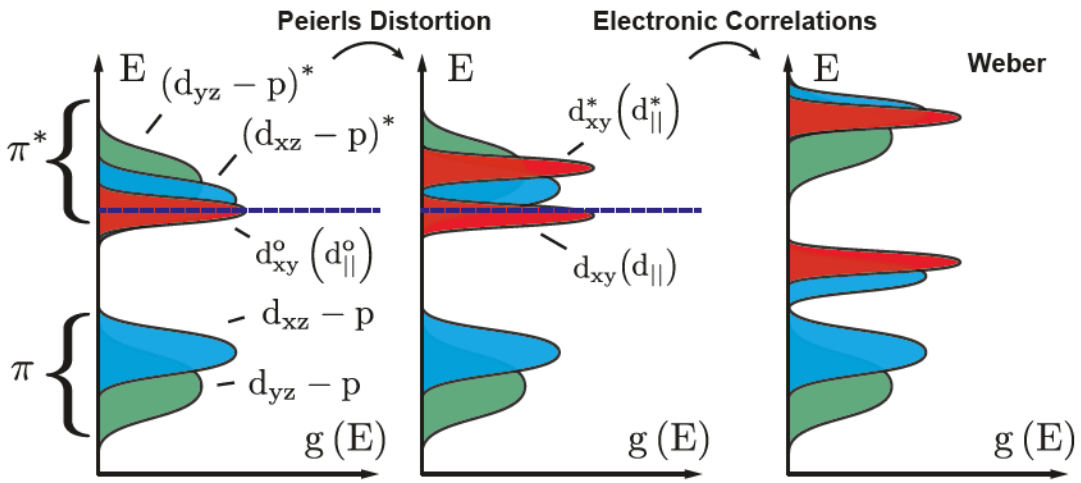

Figure 3–5: The relative effects of lattice distortion and electron-electron correlations on VO_2's spectral function as predicted by the dynamical mean field theory treatment of Weber *et al.* [31]. This figure is based on a personal communication with Cedric Weber.

Weber *et al.* [31] attempt to open a gap with a cluster dynamical field theory treatment where the dominant interaction is intra-vanadium-ion correlations. In contrast to the Biermann and Goodenough pictures, Weber's study allows multi electron occupation of the d subshell. This is expected by virtue of the bands'

hybridization with the ligand p orbitals, and is supported by experimental studies [32]. Weber's simulations find equal sharing of the d subshell electrons between d_{xy} ($d_{||}$) and d_{xz} with d_{yz} mostly unoccupied in the M_1 phase. This double occupancy on each Vanadium site in turn leads to strong correlation (hence localization) effects. A schematic of the spectral function implied by Weber's picture is given in Fig. 3–5

3.2.2 Contemporary experimental studies of VO_2

Modern experimental studies of VO_2 have attempted to use the material's equilibrium phase diagram to understand the roles of interactions leading to its low temperature behavior, and have leveraged powerful modern techniques to map its electronic structure in exquisite detail. With the maturation of ultrafast methods, it has also been shown that the phase transition may be driven optically, in a highly nonequilibrium sense.

Equilibrium phase transition

Two main classes of experiments on VO_2's equilibrium phase transition have advanced our understanding of the material and of the nature of the structural and electronic reorganization that occurs at T_c. Several x-ray absorption spectroscopy studies (and complimentary photoemission spectroscopy) clarify VO_2's spectral function near the fermi level in both equilibrium phases. Recently, a set of near-field infrared microscopy studies, performed in Dimitri Basov's group at UCSD, have attempted to identify non-congruence in the structural and electronic phase transitions.

Accommodated by advances in soft x-ray techniques, Abbate *et al.* [33], published a soft x-ray absorption study of VO_2's low and high temperature phases in 1991. With 100 meV resolution this study showed that during the upon cooling to the low temperature phase, a feature consistent with an upper Hubbard band forms

above the t_{2g} anti bonding orbitals (see Fig. 3–6 A and B). More recent studies confirm and expand upon this finding. Haverkort *et al.* find polarization dependent x-ray absorption spectra in the insulating phase [32], as show in Fig. 3–6 C. This anisotropy is in keeping with the augmented occupation of the quasi-one-dimensional $d_{||}$ band discussed earlier.

In a followup photoemission spectroscopy report, the same group identifies a satellite peak in the metallic valence band [34]. The binding energy of this peak (Fig. 3–7), greater than that of the insulator's valence band suggests that traditional single band correlations cannot adequately describe the phase transition. In such a one band Mott-Hubbard system the satellite peaks of the conductive phase spectra grow into Hubbard bands of higher binding energy through the metal to insulator transition. The authors of these studies conclude that the transition must hinge on a multi-band orbital selective mechanism beyond standard Peierls or Hubbard physics. Both [30] and [31] predict the major features of VO_2's electronic structure identified by the spectroscopy community.

The other important class of experiments on the equilibrium phase transition explore its spatially resolved character. Near-field infrared microscopy studies [35, 36], able to resolved optical properties with 100 nm precision, reveal a percolative transition to the metallic phase through the transition temperature [35]. Subsequent work revealed similarly percolative behavior in the structural phase transition [37]. Qazilbash *et al.* calculated insulating and M_1 phase fractions based on these spatial resolved techniques and noted a possible non-congruence between the electronic and structural transitions (Fig. 3–8). Evidence of cooperativety, by virtue of fine temperature and conductivity resolution in a conventional probe measurement, has also been reported recently [38]. Together these works suggest that long range order

exists in the electronic degrees of freedom for the low temperature phase and that the electronic phase transition *may* be decoupled from the structural phase transition at equilibrium.

Ultrafast studies of VO_2

With the advent of robust femtosecond laser systems, a number time resolved studies of VO_2 have also been performed. The first study, published in 1994 [39], identified the photoinduced semiconductor metal phase transition in VO_2 with sub 500 fs time constant. Becker *et al.* noted that this time scale implies a nonequilibrium mechanism for the phase transition. Subsequent ultrafast experiments have aimed to elucidate this mechanism by characterizing the time evolution of both the crystal lattice and the accompanying electronic structure.

A series of papers by Andrea Cavalleri and coworkers explored VO_2's coupled electronic and lattice structure through the photoinduced phase transition. The first paper of the series presented time resolved x-ray diffraction measurements confirming that the photoinduced phase transition first measured by Becker drives VO_2 through a structural reorganization to the equilibrium rutile lattice. The major result of this paper is presented in Fig. 3–9—the τ_{P-p} dependent magnitude of a Bragg peak associated with the M_1 structure for a pump fluence of $\Phi = 25$ mJ/cm^2. Their next paper is the time resolved analogue of [33]. This work observed a suppression of the 516 eV 2p absorptivity through the photoinduced phase transition. The photoinduced absorptivity suppression—at the conduction band satellite peak—is similar to those observed through the equilibrium phase transition. Thus, these results suggest that the photoinduced phase has a similar electronic structure to the equilibrium high temperature phase.

In the same year, Cavalleri *et al.* published a near IR time resolved reflectivity study. This work resolved an oscillatory response in the infrared reflectivity, shown in Fig. 3–10 (1A). The inset of the figure shows the residual Fourier transform. As shown in panel 1B, the oscillatory feature maps onto the spectra of the phonons that map the M_1 and R structures. The authors conclude that the role of the lattice is deterministic in the formation of a metallic phase, and that, as a corollary, the low temperature insulator is band-like. Further, they find that, for increasingly impulsive pump durations, there is finite sub-hundred-femtosecond bottleneck in the transition rate. The authors take this to suggest that there is a structural bottleneck in the photoinduced semiconductor to metal transition.

Recently, a comprehensive pump probe reflectivity study by Simon Wall *et al.* further explored the coherent excitation of these modes (Fig. 3–10 (2)). Significantly, the authors found long lived coherent excitation of the modes only below a pump threshold associated with a change in lattice symmetry. At fluences well above the phase transition threshold, they find no evidence of coherent excitation of monoclinic phonons. Below the transition threshold, they found that the application of a second pump pulse in (or out of) phase with this excitation augmented (or suppress) the measured coherent response. Above the transition threshold, they found no such phase dependence. The authors note that the photoinduced melting of other Peierls-distorted materials occurs on subphonon-period timescale. They conclude that coherent excitation of M_1 modes is not the mechanism of the ultrafast structural phase transition, noting as primary evidence the disparate responses of the excited state above and below the phase transition threshold.

The maturation of ultrafast electron diffraction and time resolved terahertz spectroscopy instrumentation in the past decade has naturally lead these methods to be

applied to VO_2's photoinduced phase transition. In 2007, Baum *et al.* published an ultrafast electron diffraction measurement of the photoinduced VO_2 phase transition [44]. This measurement identified a ∼307 fs time constant associated with the disruption of the vanadium vanadium and a ∼9.2 ps time constant associated with the rotation of the dedimerized pairs to the rutile axis. Additionally the authors observed a pump fluence threshold between 4 and 8 mJ/cm^2 for the transition, in keeping with previous work. Baum's study compliments the earlier work by Cavalleri [42] by characterizing the nature of optically induced structural changes in VO_2. The major results of this paper are presented in Fig. 3–11.

Finally, a small number of time resolved terahertz spectroscopy studies have been performed on VO_2. In 2007, two studies of the phase transition, one at low fluence and one at higher fluence, were published [45, 46]. Hilton's work found a threshold fluence for the near direct current conductivity of ∼7 mJ/cm^2 at 300 K (see Fig. 3–12 1). Further, the authors found that, for basal temperatures approaching T_c, the susceptibility of samples to the photoinduced phase transition was drastically increased. Near the equilibrium transition temperature the threshold fluence was reduced, but never eliminated (Fig. 3–12 2), suggesting that the threshold fluence is associated with the specific heat of the structural transition. In contrast to Hilton *et al.*, Kubler *et al.* (and subsequently Pashkin *et al.*) were able to characterize VO_2's coherent response below the structural phase transition threshold [46, 47]. For sufficiently low temperatures, and below the structural phase transition threshold, Pashkin and Kubler find evidence of the coherent excitation of the previously discussed 6.1 THz by virtue of its effect on the activity of higher frequency dipole active modes. The

authors also infer a nonlinear coupling (proportional to the square of the rutile normal coordinate) of electronic excited states to the 6.1 THz A_g mode. The evidence for these conclusions is presented in Fig. 3–13.

The summarized time resolved works represent significant progress towards our understanding of VO_2's photoinduced phase transition, but are by no means conclusive. While Pashkin, Hilton, *et al.* propose that coherent excitation of M_1 modes is the mechanism of the structural phase transition, Wall *et al.* provide evidence to the contrary. Only two diffraction studies directly characterize photoinduced structural phase transition. Cavalleri *et al.* measured only a single Bragg peak characteristic of the M_1 phase as evidence of the lattice changes. Though the work of Baum *et al.* characterized complete time resolved diffraction signatures, it was performed in a reflection geometry making it susceptible to surface specific effects. Conclusively deterring the roles of carrier relaxation, lattice structure, and electron electron correlation effects in VO_2's optically induced phase transitions remains an open goal of the subfield.

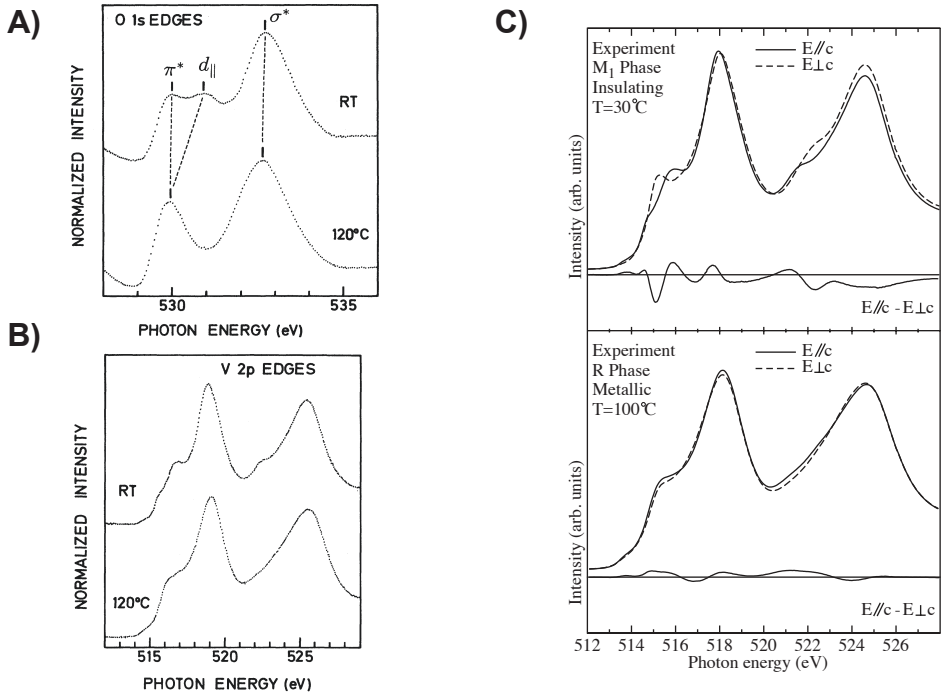

Figure 3–6:
A) O 1s absorption spectra of VO_2taken at room temperature and at T = 120 °c. Figure 2 of [33]
B) V 2p absorption spectra of VO_2taken at room temperature and $T = 120$ °C. Figure 3 of [33]
C) Experimental V $L_{2,3}$ XAS spectra of VO_2in the insulating M_1 phase (top panel, $T = 30$ °C) and metallic R base (bottom panel, $T = 100$ °C), taken with the light polarization $\vec{E} \,||\, c$ (solid lines) and $\vec{E} \perp c$ (dashed lines). The metal-insulator transition temperature is 67 °C. Figure 3 of [32]

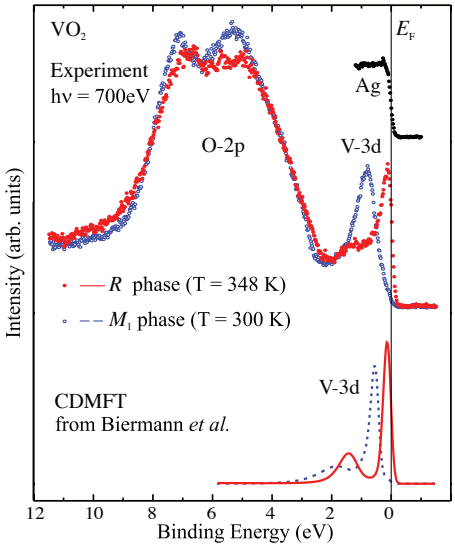

FIGURE 3–7: Top: Valence band photoemission spectra of VO_2 taken at 300 K (insulating M_1 phase) and 348 K (metallic R phase) with 700 eV photons, together with the Ag fermi level E_F reference. Bottom: CDMFT results for the V $3d(t_{2g})$ spectral weights from Biermann *et al.*. Figure 1 of [34]

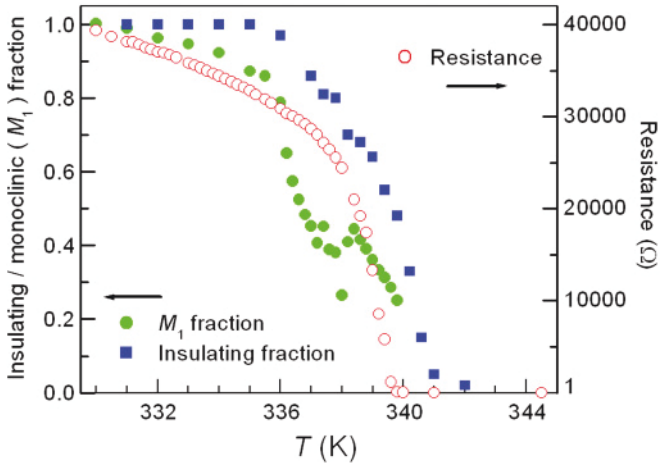

FIGURE 3–8: The fraction of monoclinic M_1 phase and the fraction of the insulating phase are plotted as a function of temperature along with the resistance of VO_2 in the SPT/IMT regime. Figure 4 of [37]

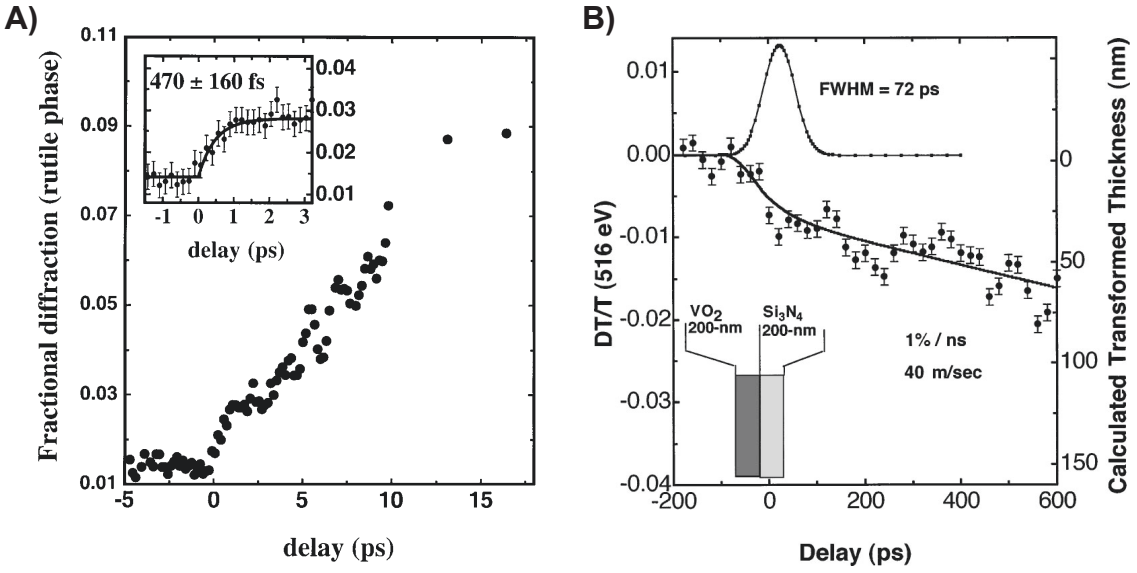

Figure 3–9:
A) Main plot: Time-dependent, integrated diffraction signal from the metallic rutile phase normalized to the integrated diffraction from the monoclinic phase. The integrals are calculated over a region of 0.1° around the center of the respective lines. Inset: Regions near zero time delay. Continuous curve: exponential fit of the rise time. Figure 3 of [40]
B) Time-resolved transmission changes at the vanadium L_3 edge. The data are fitted with a two-time-scale model, obtained by convolving a rapid and a slow response with the duration of the 70 ps x-ray pulse, as measured by cross correlation of the laser with the visible part of the synchrotron radiation spectrum. Figure 3 of [41]

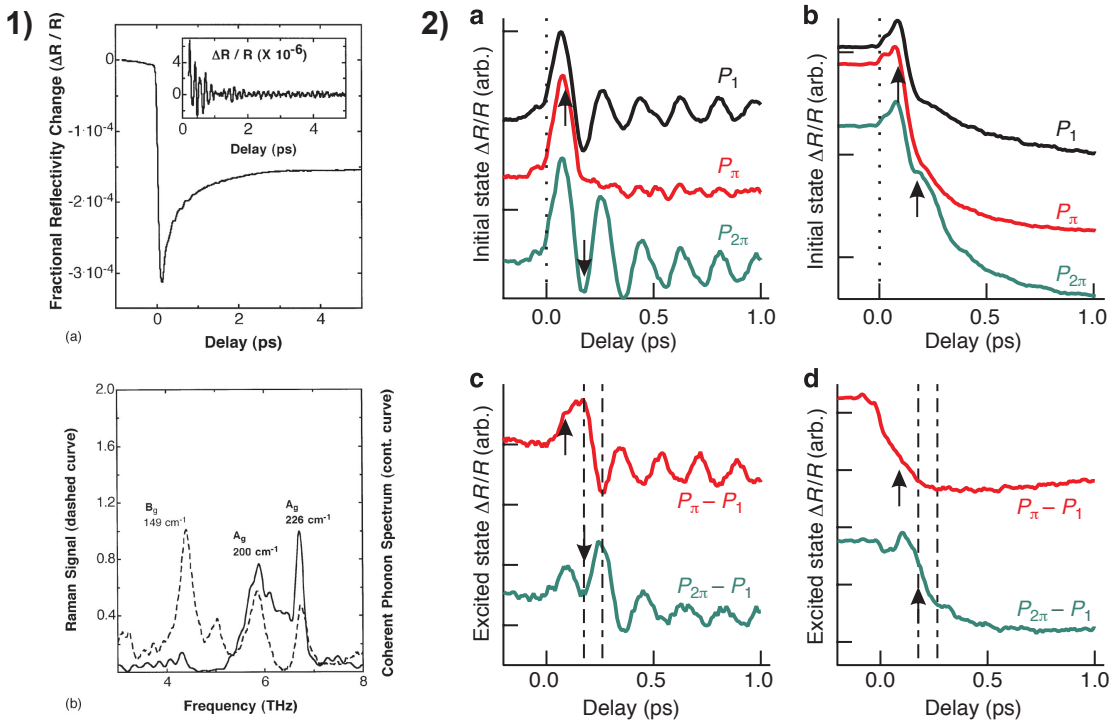

Figure 3–10:
1) (a) Time-resolved evolution of the reflectivity, measured using a Ti:Sa oscillator emitting 40-fs pulses at 850 nm. The inset displays the oscillatory part of the signal, obtained by subtracting the background. (b) unpolarized, continuous-wave Raman spectra (dashed curve), acquired in backscattering geometry using 532-nm cw excitation. The modes at 5.85 Thz and 6.75 THz are fully symmetric A_g modes, while the lower mode is of B_g symmetry. The continuous curve: Fourier transform of the time-resolved oscillations, revealing the coherent exception of the A_g modes only. Figure 4 of [42]
2) Pump-pump-probe measurements (a) below threshold and (b) above. Traces labelled P_1 correspond to the transient reflectivity generated by a single pump pulse. Traces labelled P_π and $P_{2\pi}$ correspond to a double-pulse excitation whiten the pump-probe delay is set to be out of phase, P_π, or in-phase, $P_{2\pi}$, with the 5.7-THz phonon mode. The arrows indicate the arrival time of the second pump pulse. Panels **c** and **d** correspond to the transient response of the excited state below and above threshold, respectively, obtained by subtracting the single-pulse transient reflectivity from the double-pulse transient reflectivity. Dashed lines correspond to the points separated by half of the 5.7-THz phonon period, which are anti correlated below the threshold and exhibit no correlation above the threshold. Figure 4 of [43].

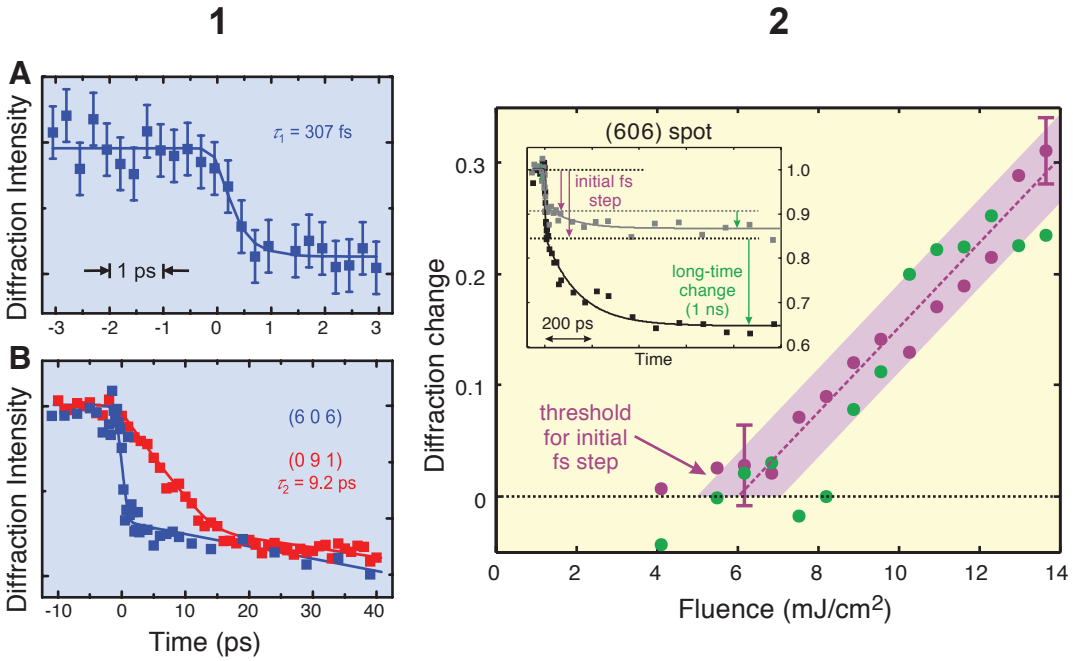

Figure 3–11:
1) Ultrafast, fs and ps, diffraction dynamics of the structural phase transition. (A) Intensity changes of the (606) Bragg spot with time. A decay with a time constant τ_1 of 307 fs was obtained on the total timescale of ± 3 ps; note the change in intensity of diffraction in the 250-fs steps. (B) Intensity changes of (606) (blue) and (091)) (red) spots with time. For all investigated Bragg spots, two different types of dynamics were observed: a femtosecond decay similar to the blue trace was measured for (806), (826), (8$\bar{2}$6), (846), (8$\bar{4}$6), (606), (714), (4$\bar{1}$7), (10 2 4) and (6$\bar{2}$8); a decay with constant τ_2 of 9.2 ps, similar to the red trace, was measured for (091), (084), and (08$\bar{2}$), on the total time scale of 40 ps. The temporal range values (Δt_1 and Δt_2) over which the decay is pronounced are 760 fs and 15 ps. This difference indicates a stepwise mechanism for atomic motions. Figure 2 of [44]
2) Dependence of the fs dynamics and the large-scale shear displacement on excitation fluence. The magnitude of the initial intensity decrease (violet) and the amplitude of the long time change (green) are plotted for different excitation fluences. A common threshold region is observed. (Inset) Transients of the (606) Bragg spot for two different excitation fluences The magnitudes of change were measured at 10 ps and 1 ns. Figure 4 of [44]

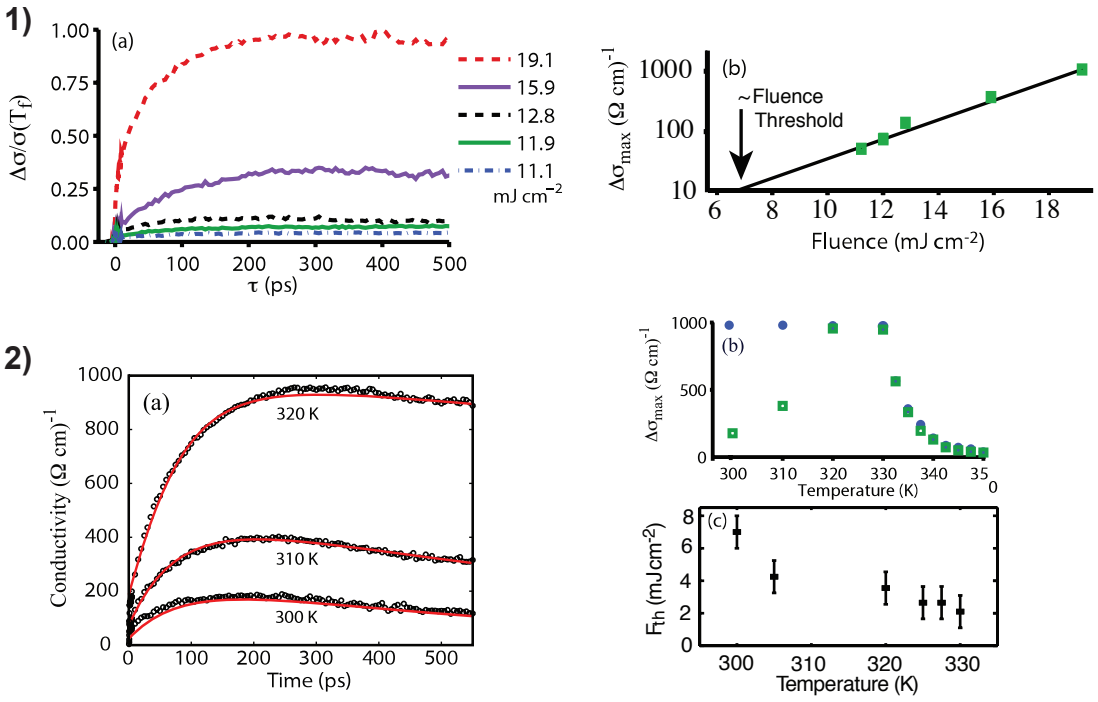

Figure 3–12:
1) (a) Photoinduced conductivity change at 300 K for various fluences where $\sigma(T_f)$ is the conductivity in the full metallic state. (b) Magnitude of the conductivity change as a function of fluence at 300 K.Figure 2 of [45]
2) (a) Induced conductivity change as a function of time at a fluence of 12.8 mJcm^{-2} for various initial temperatures. (b) Magnitude of the induced conductivity (□) and the maximum possible conductivity change (○). The black lines are a fit as described in the text. (c) Fluence threshold as a function of base temperature. Figure 3 of [45]

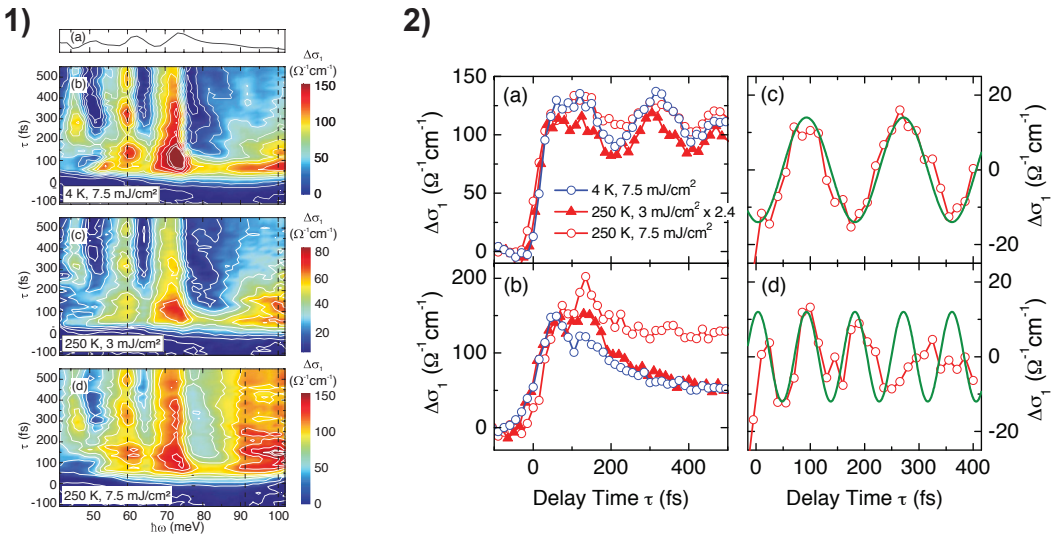

Figure 3–13:
1) 2D optical pump-multi-THz probe data: (a) Equilibrium conductivity of insulating VO_2 at 295 K. Color plots o the pump-induced changes of the conductivity $\Delta\sigma_1(\omega,\tau)$: (b) at $T_L = 4$ K and an incident fluence of $\Phi = 7.5$ mJ/cm^2; at $T_L = 250$ K and pump fluence (c) $\Phi = 3$ mJ/cm^2 and (d) $\Phi = 7.5$ mJ/cm^2. The broken vertical lines indicate the frequency positions of cross sections reproduced in Fig. 7 (Panel 2 of this figure in this thesis). Figure 6 of [47]
2) Cross sections of Fig. 6 (panel 1 of this figure in this thesis) along the time axis τ for a photon energy of (a) $\hbar\omega = 60$ meV and (b) $\hbar\omega = 100$ meV. The curves taken at $\Phi = 3$ mJ/cm^2 are scaled up by a factor of 2.4. (c) and (d) The oscillating components of the cross sections through the 2D scan in Fig. 6(d) for a photon energy of (c) $\hbar\omega = 60$ meV and (d) $\hbar\omega = 92$ meV. Green solid lines: (c) fit of the oscillating component by a cosine function with frequency of 6.1 THz, (d) the fitting function shown in panel (c) squared with subtracted constant background. The oscillation occurs at a doubled frequency of 12.2 THz. Figure 7 of [47]

3.3 Chapter summary

In the late 1950s, VO_2 was discovered to have a peculiar hysteretic semiconductor to metal phase transition near 340 K. The hysteresis suggested that magnetic order was not the mechanism affecting insulating behavior in the low temperature phase. In the 1970s, Mott and Goodenough published competing theoretical models of the semiconducting low temperature phase. Goodenough argued that the periodic lattice distortion of the low temperature phase opened a gap at the Fermi surface while Mott posited that electron electron correlations in the narrow d bands about the Fermi surface were fundamentally responsible for the low temperature insulating behavior. Modern numerical treatments [30,31] conclude that electronic correlations play a dominant role in low temperature VO_2's gap formation, but that [25] the periodic lattice distortion significantly modifies the materials' electronic structure, making it susceptible to the semiconductor metal transition. Photoemission and x-ray absorption studies support the correlated character of the low temperature phase. Recently, near field infrared microscopy, and spatially resolved diffraction techniques have been used to explicitly reveal the percolative nature of the transition and the possible non congruence of the structural and electronic components of the phase transition in temperature [35,37,48].

Over the past two decades, VO_2 has also emerged as a canonical material for study by ultrafast techniques. The phase transition has been shown to be photoinducable [39], with a time constant of $\mathcal{O}$[100 fs]. X-ray absorption and time resolved photoemission spectroscopy have shown that, for sufficient fluences, the photoinduced state is indisputably the equilibrium high temperature state [40–42]. Ramman and

time resolved terahertz spectroscopy studies have suggested that coherent excitation of the phonons around 6.1 THz, which maps the low temperature and high temperature structures, as the mechanism for the nonequilibrium phase transition.

The current areas of interest in the VO_2 subfield are: (a) confirming and characterizing the intermediate state of the equilibrium phase transition; (b) observing or eliminating the possibility of structural and electronic noncongruence in the photoinduced phase transition; and (c) determining the mechanism of the photoinduced structural phase transition. The novel work presented in this thesis represents significant progress in areas (b) and (c).

CHAPTER 4

Ultrafast electron diffraction of vanadium dioxide

The following chapter is based on a manuscript [49], in review at *Science*, for which I played an integral role in analysis and interpretation. The ultrafast electron diffraction experiments were performed by Vance Morrison, as was the extraction of diffraction signatures from raw data. My role extended to attribution of physical mechanisms to particular diffraction signatures, understanding the implications of these signatures to the modern understanding of VO_2's low temperature phase, writing a significant portion of the manuscript, and making Figures 1A, 1B, and 4A. In addition I performed equilibrium TEM measurements on the samples; these data aided in the normalization of the UED data presented. Dr. Chatelain, the second author, built the diffractometer with Dr. Morrison. Andrew Bruhacs assisted Dr. Morrison in the acquisition of infrared transmissivity data. Ali Hendaoui synthesized the VO_2 thin films. Finally, Professors Bradley Siwick and Mohammad Chaker supervised the research.

4.1 Experimental

4.1.1 Samples

70 nm polycrystalline VO_2 samples were prepared via pulsed laser deposition on 50 nm amorphous Si:N membranes. Sample synthesis and equilibrium characterization was performed at the Institut National de la Recherché Scientifique Centre Énergie Matériaux Télćommunications facility by Ali Hendaoui. The synthesis protocols are detailed in a separate publication [50]. Fig. 4–1 shows the conductivity hysteresis measured for a sample witness to the batch used in this chapters' experiments—it is in good agreement with literature accounts of VO_2. A transmission electron micrograph, and a characteristic diffraction signature is given in Fig. 4–2 in addition to a schematic highlighting relevant structural metrics.

4.1.2 Experimental parameter space

Ultrafast electron diffraction measurements were performed in accordance with the methods of Chapter 2 between 0 and 30 mJ/cm^2. A 35 fs, 1.55 eV pump pulse was used to induce a sample response in conjunction with while a 350 fs probe pulse of ∼500,000 95 keV electrons. Data were taken at a repetition rate of 50 Hz to allow proper cycling of the VO_2 samples back to initial conditions. Such a slow repetition rate was necessary as the 10^{-7} mbar pressure decouples the sample from most possible thermal reservoirs. In turn, this hinders the sample's return to initial conditions after each pump cycle. The probe pulse had 10° incidence to the film surface, while the probe pulse was transmitted at normal incidence.

4.1.3 Infrared transmissivity

Ultrafast infrared transmissivity measurements were made in concert with ultrafast electron diffraction. The probe pulse was generated through difference frequency

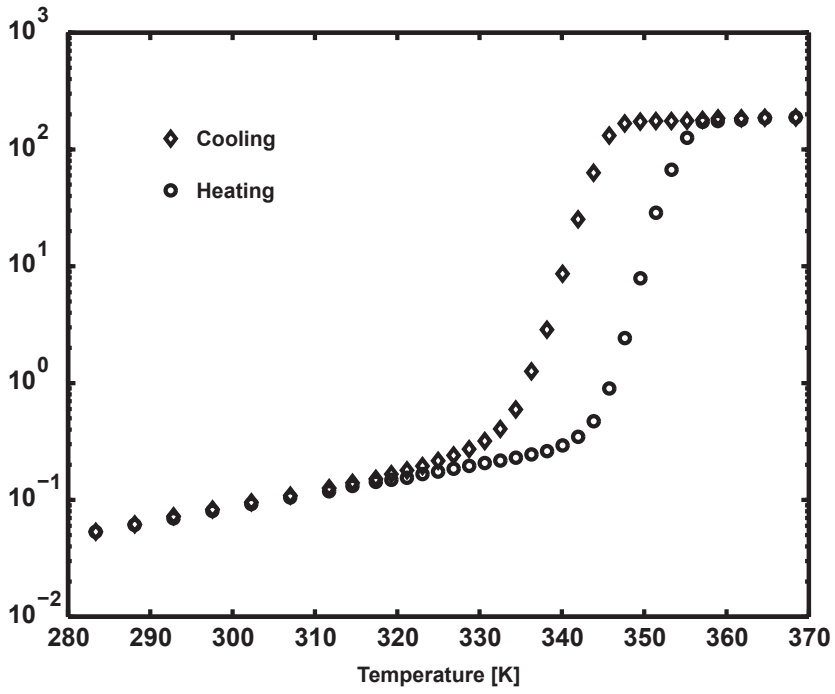

Figure 4–1: Four point conductivity measurement performed on a sample witness to transmission electron microscopy samples' synthesis process. A hysteresis of 9.5 K was measured about a transition temperature of 344.7 K.

generation in an optical parametric amplifier. Measurements were performed under identical pump conditions (including angle of incidence) using a 248 meV probe pulse. These measurements were performed at 760 torr of N_2, with a repetition rate of 50 Hz. A spectrometer from Infrared Systems Development based on a 64 pixel mercury cadmium telluride IR detector array was used.

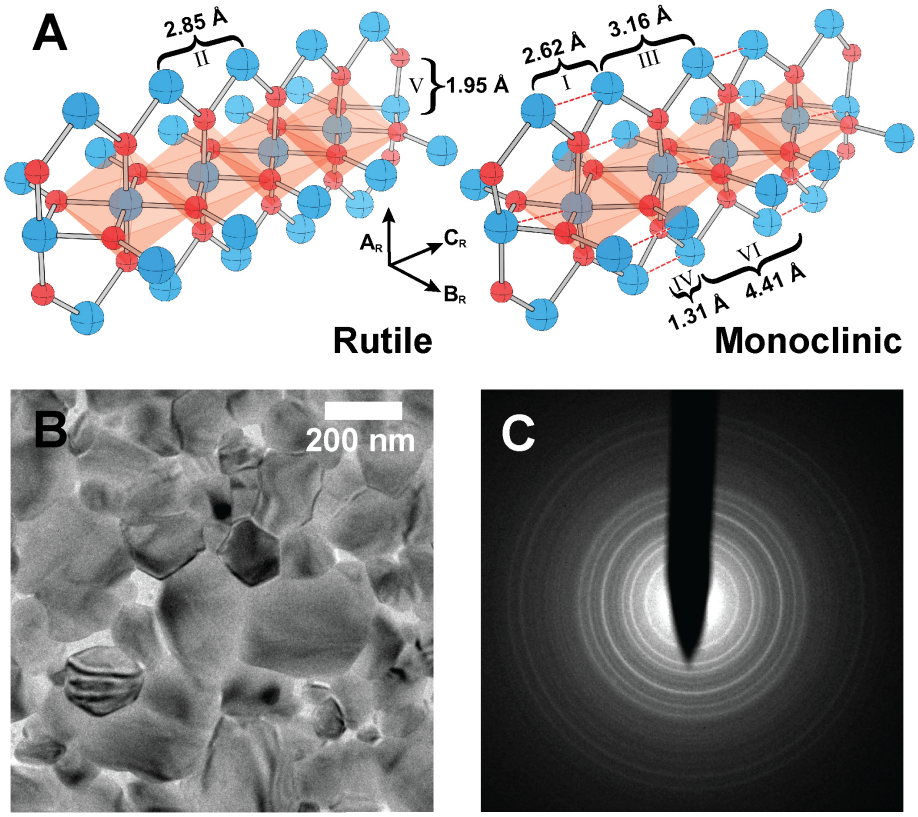

Figure 4–2: A) The structure of rutile VO_2 (left) and monoclinic VO_2 (right). B) Transmission electron microscopy image of the pulsed laser deposition grown VO_2 sample used in these studies. C) Example electron powder diffraction pattern of the monoclinic phase. Figure 1 of [49]

4.2 Results

Raw data takes the form of 2048 × 2048 images from the CCD indexed by pump probe delay. Diffraction signatures are extracted from these images by fits to peaks (rings) and the diffuse background. From the pump probe delay dependence of these diffraction signatures, one may infer the photoinduced crystallographic changes in the sample. Mid infrared transmissivity measurements in the same fluence domain accompany compliment the diffraction measurements.

The major results of this experiment are presented in Fig. 4–3. The left column of the figure presents diffraction data for $\Phi = 20$ mJ/cm^2. The signature in panels A and B consists of three basis components: a time dependent diffuse background, and two diffraction signatures with disparate time scales. Panel E gives the first 1.5 ps of differential diffraction dynamics—the red lines indicate peaks allowed in the M_1 phase but not the rutile phase ($30\bar{2}$, $12\bar{2}$ and $31\bar{3}$). A fast $\tau_S \simeq 300$ fs signature dominates the total diffraction in this regime, and associated with the structural phase transition. After a short, 1.5 ps, time delay, slower dynamics, $\tau_E \simeq 1.6$ ps, dominate the differential diffraction signature. These dynamics, shown in panel F, do not have an interpretation in terms of a structural phase transition. For reciprocal lattice vectors perpendicular to $\mathbf{c}_R$, slow dynamics are not observed.

To understand the fluence dependence of these signatures, the amplitude of features characteristic of each signature ($30\bar{2}$ for the fast dynamics and 220 for the slow dynamics) were tracked over a range of fluences. Linear fits suggest threshold fluences of $\Phi_S = 9$ mJ/cm^2 for the structural fast dynamics and $\Phi_E \simeq 2$ mJ/cm^2. Importantly, the changes below Φ_S are long lived, and therefore represent an astructural transition to a metastable phase in at least some subset of the sample volume. Infrared transmissivity measurements suggest that the pseudogap in this state smaller than 250 meV. Diffraction signatures for $\Phi = 6.1$ mJ/cm^2, well below Φ_S are given in Fig. 4–4.

4.2.1 Pair distribution function analysis

The pair distribution function, effectively an autocorrelation of the potential, may be used to glean real space information about the transition [51]. A peak for a particular r in the pair distribution function means that the potential has significant magnitude at at least two points, separated by r within the unit cell.

The differential pair distribution function, given for $\Phi = 20$ mJ/cm^2 in Fig. 4–5, may be interpreted accordingly. For $\Phi > \Phi_S$ the structural phase transition is clearly evidenced in the pair distribution function (Fig. 4–5 A) by negative going features at the dimerized inter vanadium distances and a positive going feature at the rutile vanadium vanadium separation. These dynamics, corresponding to Fig. 4–3 E, are completed within the first two picoseconds of photo excitation. The astructural signature (dynamics in Fig. 4–3 F, Fig. 4–5 B), most visible for $\tau_{P-p} > 2$ ps, is characterized by negative going features at 1.3 Å and 4.3 Å and a positive going feature at 2 Å. The two positive going features occur at the half vanadium dimer distance, and at the analogous distance to the adjacent dimer bond. The positive going feature occurs at a distance characteristic of the vanadium oxygen separation. These signatures are interpreted in the discussion section.

4.2.2 Heterogeneous response

Excluding their relative amplitudes, the two diffraction signatures extracted in Fig. 4–3 show mutual indifference over the fluence domain explored. That the low threshold signature is unchanged above the 9 mJ/cm^2 threshold suggest that the dynamics affecting the two signatures occur in distinct sample volumes. We propose that the sample response is heterogeneous in this way. There are several potential sources of this heterogeneous response. Crystallite orientation within the film, local variations in sample stress, or even the statistical nature of absorption the process could all lead to differential response among distinct sample volumes. However, we cannot promote a particular one of these mechanisms based on our results. It is likely that all contribute in part.

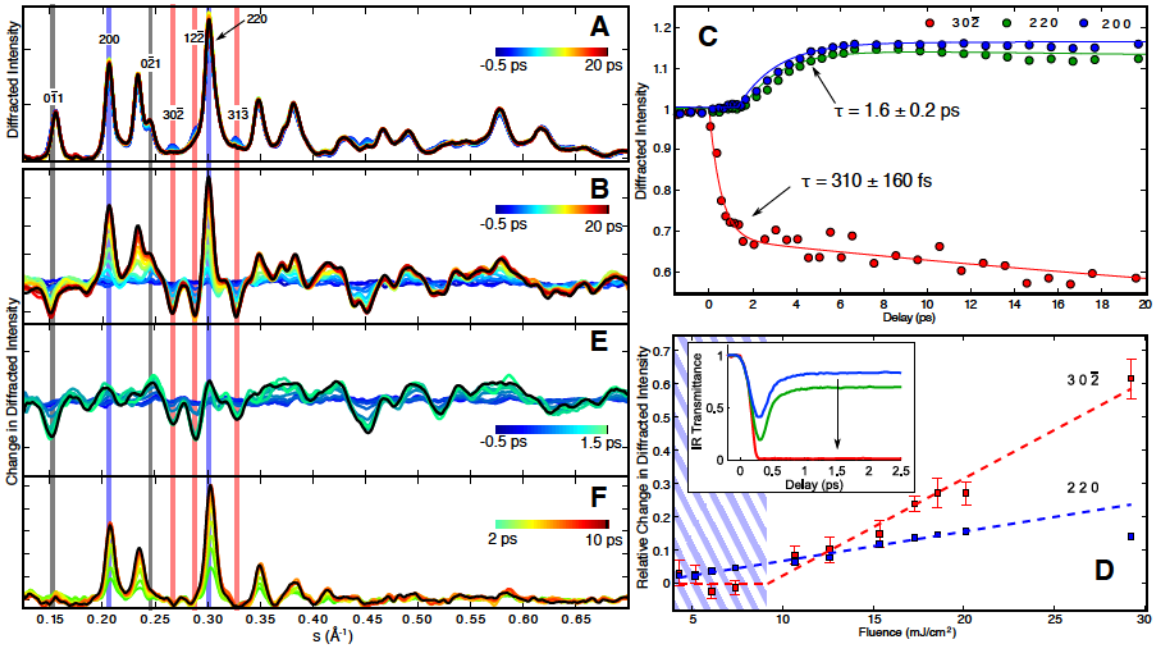

FIGURE 4–3: Structural dynamics during the SMT in VO_2. A) Raw, background subtracted, UED data from 0-20 ps. Red vertical lines indicate several weak reflections allowed in the M_1 phase due to the PLD but not in the R-phase. Blue lines indicate several peaks present in both equilibrium phases. The grey lines indicate peaks for which $h_M = 0$. B Overall diffraction difference spectrum from -0.5 to 20 ps, C) time resolved diffraction peak intensity showing fast ($\sim$ 300 fs) and slow ($\sim$ 1.6 ps) dynamics respectively for peask indicated by red and blue vertical lines in the diffraction spectra (leftmost panels). The dashed line remarks a delay of 1.5 ps and acts as a guide to the eye. D) Fluence dependence of the fast and slow signal amplitudes as measured for the $(30\bar{2})$ and (220) peaks shown in C). The range of fluences for which no SPT is observed is indicated by the hatched region. Inset) Time resolved IR (5 μm 250 meV) transmissivity in this hatched fluence region (3.7 mJ/cm^2 (red), 2.7 mJ/cm^2 (green) and 1.9 mJ/cm^2 (blue)) display a persistent decrease to a very long-lived plateau (>100 ps). The amplitude of this decrease reaches >99% at 3.7 mJ/cm^2, indicating a significant closing of the semiconducting gap and a transition to a metallic-like state. E) Diffraction difference spectrum for the fast dynamics. The change in diffracted intensity from -0.5 ps to 1.5 ps and F) Diffraction difference spectrum for the slow dynamics. The change in diffracted intensity from 2 ps to 10 ps (referenced to 2 ps) is shown. Figure 2 of [49]

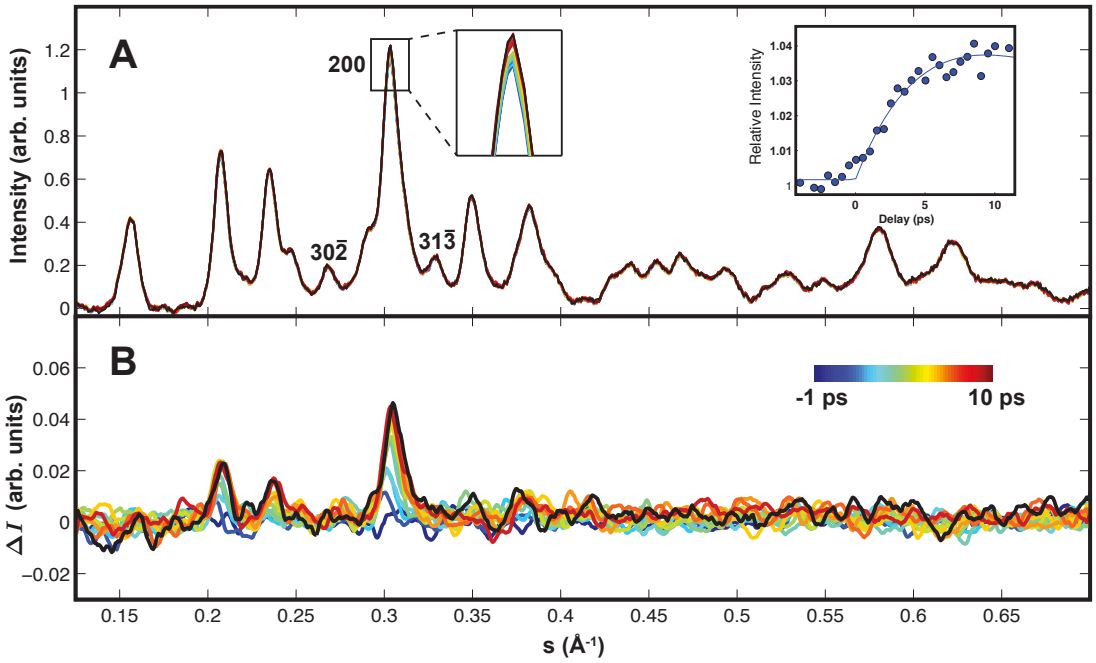

Figure 4–4: A) Time resolved, background subtracted, diffraction data from 0 ps to 10 ps and an excitation fluence of 6.1 mJ/cm^2. Inset) Time resolved intensity of the 220 reflection. B) Time resolved change in diffracted intensity shown in A). No decrease is seen in the 30$\bar{2}$ and 31$\bar{3}$ reflections, indicating that the PLD remains intact. In addition no changes are observed for $s > 0.5$ Å^{-1} region. Figure of [49]

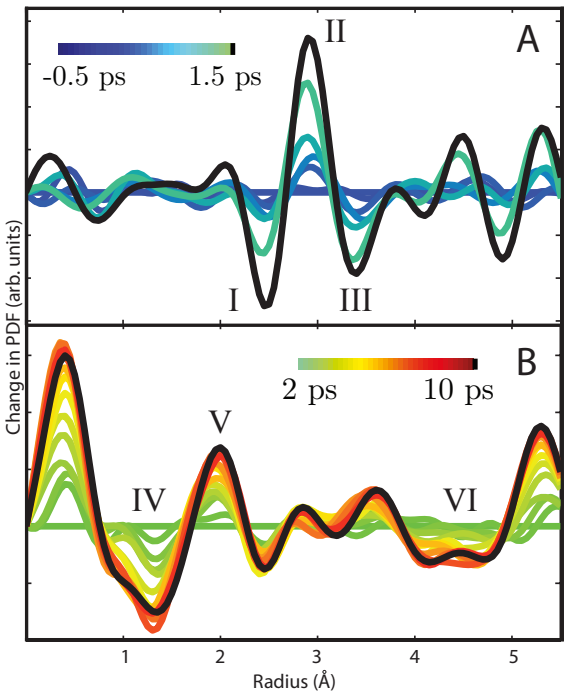

Figure 4–5: Difference pair distribution functions for the two observed characteristic time scales. A) Difference PDF from -0.5 ps to 1.5 ps referenced to -0.5 ps. B) Difference PDF from 2 ps to 10 ps referenced to 2 ps. The roman numerals correspond to the distances labeled in Fig. 4–2. Figure 3 of [49]

4.3 Discussion

These results have significant implications to our understanding of the roles of electronic and phononic instabilities in VO_2.

4.3.1 The photoinduced structural phase transition

With unprecedented signal quality, we show that, above Φ_S, the structural phase transition occurs in a single, ultrafast, step with time constant $\tau_S = 310 \pm 160$ ps. Previous time resolved structural studies [44] proposed a two step mechanism with separate lifetimes associated with the rotation of the dimers from their tilted orientation and the breaking of the dimers along $\mathbf{c}_R$. Baum *et al.* found a time constant of 307 fs associated with a relaxation of the vanadium dimers along the $\mathbf{c}_R$ axis, and a time constant of 9.2 ps associated with the rotation of the vanadium pairs onto the rutile axis. The work in [44], was performed in a reflection geometry, and we propose that the disparate time constants they measure are a surface artifact. Our measurements, from a transmission geometry, sample the entire volume of the VO_2 film, and thus provide a more accurate picture of its bulk behavior.

4.3.2 The metastable monoclinic conductor

For fluences below the 9 mJ/cm^2 threshold, we find only the diffraction signature, which is incompatible with a structural phase transition. Based on the above mentioned pair distribution function and symmetry arguments, we concluded that this signature corresponds to a valence charge redistribution within the oxygen hybridized d bands. The astructural dynamics must be a charge density rearrangement along the rutile **c** axis. Dynamical mean field theory work [31] has suggested that correlation effects, which lead to population redistributions within the t_{2g} d bands, dominate the low temperature gap. In the conducting phase, the three t_{2g} bands are

isotropically populated, while the gapped phase has population in either d_{xy} [30] or both d_{xy} and d_{xz} [31]. Our results support the Weber picture (Fig. 3–5). The negative going features in the pair distribution function at 1.3 Å and 4.4 Å are indicative of increased population in the d_{xy} while the positive going features at 0.8 Å and 1.9 Å suggest depopulation of d_{xz}. The d_{yz} orbital, orthogonal to $\mathbf{c}_R$, has no photoinduced population change. We propose that we have observed a photoinduced suppression of the formation of Hubbard bands in d_{xz} and possibly d_{xy}. The relative energies of non-correlated bands would then explain the occupation dynamics.

IR transmission spectra show that, for this fluence domain, the IR conductivity of the effected sample increases by several orders of magnitude. Furthermore, these changes persist for hundreds of picoseconds, demanding the existence of a metastable (or stable) monoclinic conductive phase of VO_2.

Based on our measurements, the mechanisms affecting the large value of τ_E and the stability of metallic monoclinic phase remain open questions. The slow time constant is characteristic of lattice heating processes [52], suggesting that the disruption of correlation effects may be thermal. In keeping with this interpretation, the long lived nature of the state would then be affected by a bottleneck in the dissipation of heat from the sample. However, as we were not able to extract lattice temperature from Debye-Waller type analysis, we are not in a position to rule out kinetic arguments for the lifetime of the state (e.g. a bottleneck in phase space separating the low temperature and metastable states). We note the possible connection of monoclinic metallic phase of this study to the equilibrium conductive puddles observed by Qazilbash et al. [35]. Further evidence of this state was reported by Nag *et al.*, who report a non congruence in the equilibrium electronic and structural phase transitions.

4.3.3 Conclusions

Our results provide a novel perspective to the decades-long discourse on VO_2. We have conclusively shown the existence of a long lived phase with conductive infrared properties, but the lattice structure of the insulator. The existence of this phase dictates that the periodic lattice distortion is not the dominant gap forming mechanism. Instead, we conclude that the role of the lattice distortion is to modify the energy (occupation) of the t_{2g} bands. In the presence of the monoclinic structure, the d_{yz} band is destabilized, and the remaining anisotropic t_{2g} bands become susceptible to correlation effects. Importantly, we show that the isotropic electronic structure of the high temperature phase does not form in the presence of the lattice distortion.

These results are also important from an instrumentation perspective. Traditional transmission electron diffraction has been demonstrated as a probe of valence charge density [53, 54]. These data are the first evidence that time resolved electron diffraction may be used as an analogous probe of dynamical valence charge density behavior.

CHAPTER 5

Time resolved terahertz spectroscopy of vanadium dioxide

Time resolved terahertz spectroscopy was performed on identically prepared samples in the same fluence regimes. The aim of these experiments was to determine the near direct current conductivity of the metastable photoinduced phase reported in Chapter 4. Terahertz spectroscopy has been shown to characterize the Drude-like conductivity of traditional photodoped semiconductors [36]. Thus it is naturally an interesting probe to understand the character of the electronic changes affected by photo excitation in more complicated materials such as VO_2. Characterization of the low frequency spectroscopy of the novel metastable state described in Chapter 4 will allow a better understanding of the role of lattice structure in determining low temperature VO_2's electronic properties.

The experiments presented in this chapter were performed by myself and David Valverde. Data analysis and interpretation was preformed by myself under the supervision of Prof. Cooke and Prof. Siwick.

5.1 Experiment

5.1.1 Samples

Samples were prepared using pulsed laser deposition in an identical manner to those used in in Chapter 4. As in Chapter 4, four point probe measurements confirm the films' insulator metal transition at 342 K with a hysteresis of 8.5 K Fig. 5–1.

5.1.2 Time resolved terahertz spectroscopy setup

A schematic of the THz time domain spectroscopy (THz TDS) apparatus used is given in Fig. 5–2. The methods indicated in Section 2.3 were used for THz pulse generation from a 40 fs, 800 nm seed (identical to the pump). The probe pulse waveform and power spectrum are given in Fig. 5–3. From 2–14 THz there is sufficient probe power to reliably extract the static and transient conductivity of the VO_2 film. Because of water's far IR activity, the apparatus is contained within a dry air vessel. It is clear from the power spectrum that this approach yields a robust broadband probe, free of absorption artifacts.

For each τ_{P-p} and τ_{THz}, both the average transmitted THz signal, and the difference (between pumped and unpumped) transmitted THz signal are recorded using an optical chopper on the pump line. As outlined, these data can be used to reconstruct the pumped and unpumped transmitted THz signals. Given pumped and unpumped signal for a particular state of the probe pulse, it is then possible to construct a complex differential transmission coefficient that is sample intrinsic—insensitive to super 300 ms (the integration time) drift in the ultrafast laser system. A chopper speed of 13 Hz was used with a laser repetition rate of 250 Hz.

5.1.3 Experimental parameter space

Data were taken in the fluence regime between 9 and 30 mJ/cm^2. τ_{P-p} was varied from –500 fs to 10000 fs in steps between 25 and 500 fs. For each τ_{P-p}, 220 to 260 samples of the THz wave form were taken at 10 fs spacing.

5.1.4 Analysis

Reconstruction of pump induced spectroscopic change

The possibility of multiple reflections slightly complicated the analysis. Backscattering reflections, both in the THz generation line, and in the sample, substrate, and related interfaces complicate the thin film, semi infinite substrate conductivity formulae presented earlier. Indeed, significant etalon type signature is seen in raw probe pulse following the main peak. Though reconstruction of the unadulterated signal is technically possible through a transfer matrix approach [19], the precise knowledge the sample's geometry (including the shape of the etched aperture) needed for this analysis makes it impractical. A simple and robust solution for this complication is to simply window the probe waveform to remove the reflections. This method is strictly valid so long as unreflected probe pulse and the reflected post pulses are not overlapped in time. Our probe waveform is near this regime. A windowing function of form

$$W\left(\tau_p\right) = \frac{1}{1+e^{-\frac{\tau_p-\tau_\circ^1}{\sigma^1}}}\frac{1}{1+e^{\frac{\tau_p-\tau_\circ^2}{\sigma^2}}} \tag{5.1}$$

was used with $\{\sigma^1, \sigma^2\} = \{167, 125\}$ fs. $\tau_\circ^i$ were taken to satisfy the smallest range for which $\partial_{\tau_\circ^i}\sigma_1(\omega, \tau_{P-p}) \simeq 0 \;\forall\; \omega \in [2, 14]$ THz; $\{\tau_{P-p}\}$. Notably, the signal in the range from 2 to 6 THz is unaffected by the window, suggesting that the measurement robustly captures the intrinsic near DC behavior of the photoinduced state.

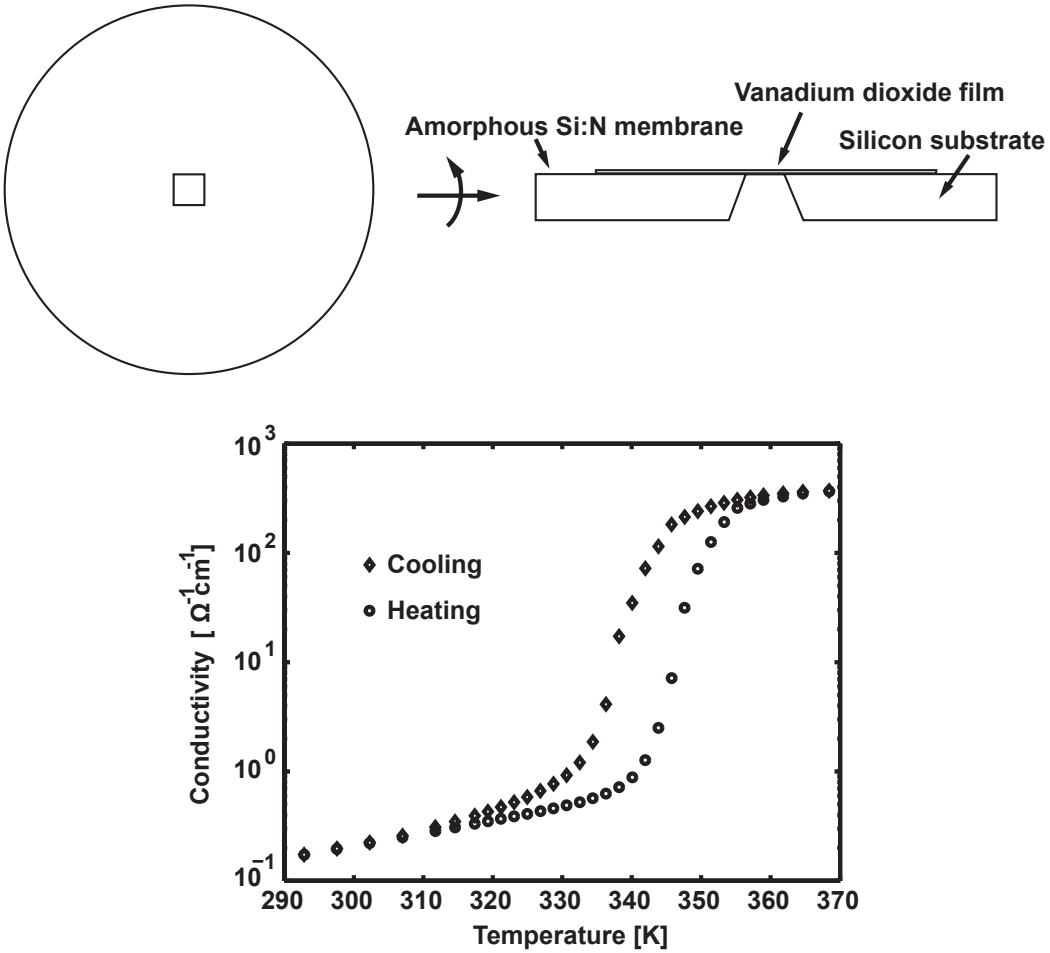

FIGURE 5–1: Schematic and characterization of the VO_2 thin films used for the experiment. Films were deposited on amorphous Si:N TEM membranes (schematic top, and photograph bottom left). Bottom right, four point measurements on witness films show the canonical equilibrium phase transition in good agreement with the literature.

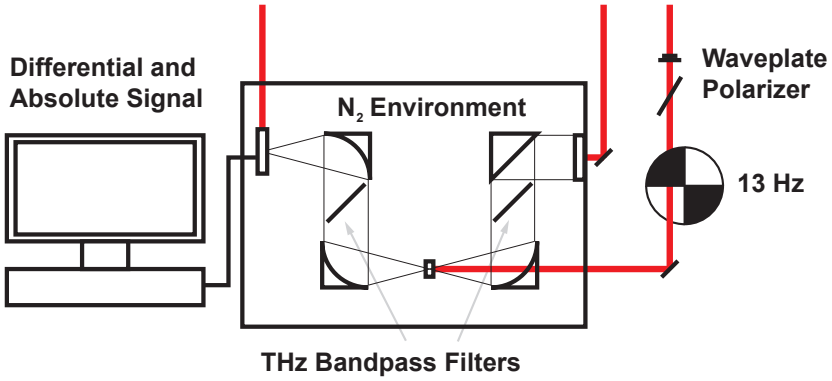

FIGURE 5–2: A schematic of the THz time domain spectroscopy setup used for the present experiment. Within a dry environment, a THz pulse is generated. A silicon wafer is used to filter the probe before it is focused through the sample position. Post specimen, the probe is columnated before being focused to the detection apparatus. The pump pulse has collinear incidence with the sample. Its power is modulated using a wave plate polarizer. A chopper in the pump line is used to allow the detection of pumped and unpumped signal for any given lab time.

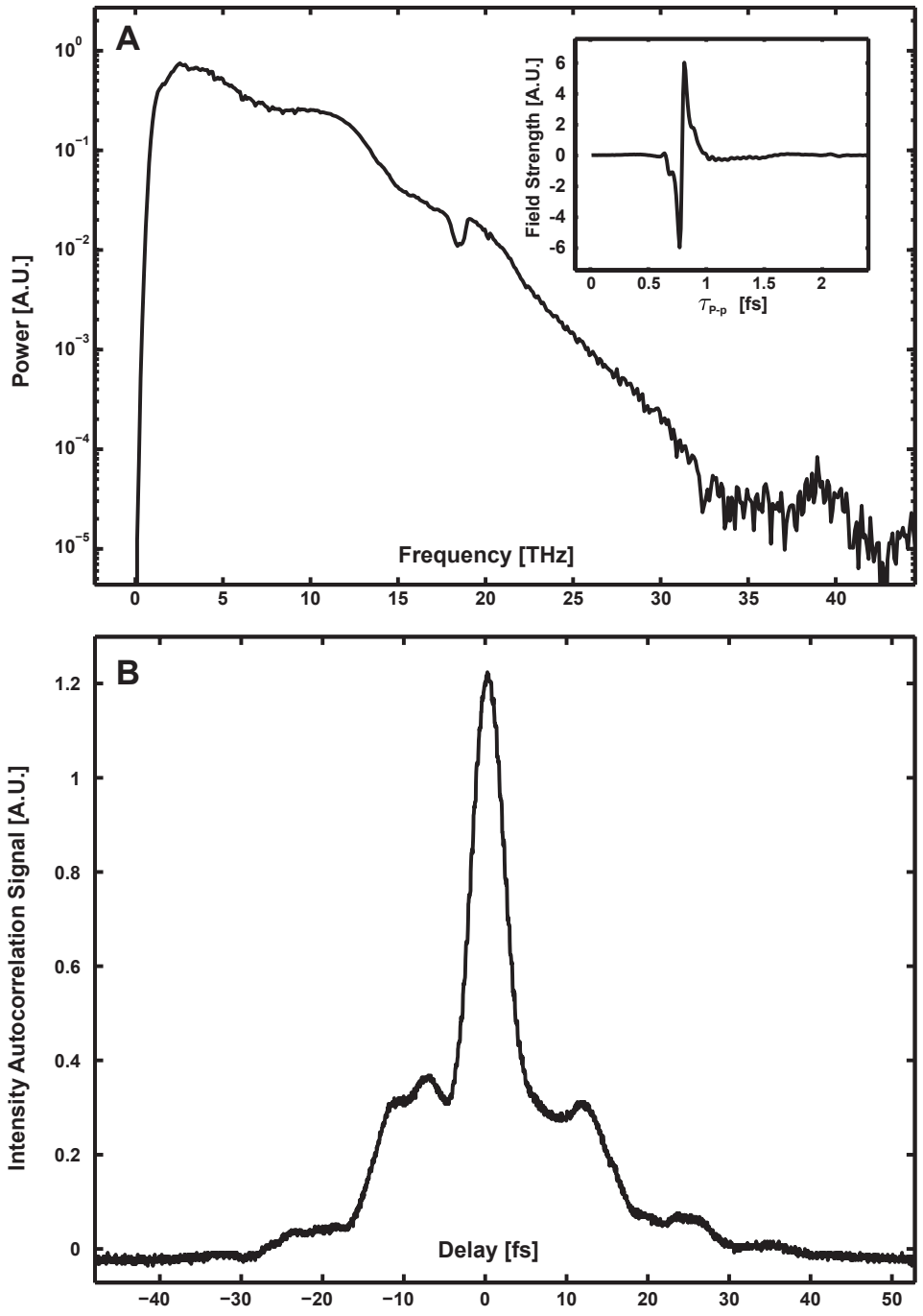

FIGURE 5–3: THz probe pulse (A), and femtosecond pump pulse (B) used for the present time resolved terahertz measurements. (A) Main panel, the probe power spectrum, in arbitrary units. Inset, the raw probe pulse wave form sampled at 10 fs intervals. (B) Intensity autocorrelation verifying the ∼35 fs duration of the pump pulse.

5.2 Results

The real τ_{P-p} dependent transient conductivities for $\Phi = \{13.5, 16.6, 18.4, 22.5\}$ mJ/cm^2—responses characteristic of the spectral response for all measured fluences—are shown in Fig. 5–4. The line shape can roughly be characterized by two frequency regimes: an unstructured low frequency regime, and a structured regime past ∼7 THz. These regimes are treated separately below. Since the spectroscopy of correlated materials, let alone the non-equilibrium dynamics thereof, is exceptionally complicated, the terahertz data is treated phenomenologically.

5.2.1 Direct current conductivity

The high fidelity of the data from 3 to 6 THz allows us to extract the direct current conductivity, σ_{DC} as a function of τ_{P-p}. Drude-Smith model (reviewed in Chapter 2) and linear fits were used to extract σ_{DC} with similar conclusions. Spectra at frequencies for which the differential conductivity remains well behaved in $\tau_{P-p} \leq 0$ are considered trustworthy. For low frequencies, below around 2.5 THz, the finite aperture size of the sample affects the THz transmission beyond the approximations presented in

The extracted $\sigma_{DC}(\tau_{P-p})$ was then fit with a biexponential. For intermediate fluences, it is clear that fast and slow contributions exist in the total direct current dynamics. The time constants of the biexponential were fixed to $\tau^F_{THz} = 240$ fs and $\tau^S_{THz} = 2.4$ ps—prescribed by the average τ^i_{THz} found from fits for fluences with fine τ_{P-p} sampling—and fits were performed to extract the relative amplitudes by which these dynamics contribute to the long time direct current conductivity. As in Chapter 4, the fluence dependence of these amplitudes is revealing to the nature of VO_2's photoinduced phase transitions.

5.2.2 Spectroscopic signatures

The shape of the spectra measured for frequencies higher than ∼7 THz is quite structured. It is difficult to parse sample dependent effects from those affected by experiment geometry and probe inhomogeneity. This domain also overlaps slightly with the structured region reported by [46, 47].

It is clear from Fig. 5–4 that the Drude-Smith model fails to describe the total behavior of the sample. We suggest that conductivity in the unstructured region below 7 THz is affected primarily by free carriers, while conductivity above 7 THz is affected by a combination of phononic and mobile charge activity.

5.2.3 Fluence dependence

The fluence dependence of the contributions of the slow and fast dynamics to the total DC conductivity at long times is given in Fig. 5–6. These data were extracted by fitting a biexponential to the linearly extrapolated direct current dynamics discussed earlier. We find similar threshold fluence thresholds for both the slow and the fast signatures of around $\Phi_E^{THz} \simeq \Phi_S^{THz} \simeq 9$ mJ/cm^2. This threshold is consistent with that observed for the structural phase transition in Chapter 4 using ultrafast electron diffraction. The coincident threshold threshold behavior of the slow dynamics, however, is in contrast to that observed in the diffraction and mid infrared measurements. This suggests a more complicated interpretation of the metastable phase's influence on VO_2's DC conductivity is needed.

At high fluences, above ∼15 mJ/cm^2, the absolute contribution of the slow signature to σ_{DC} diminishes. By ∼26 mJ/cm^2, the total σ_{DC} behavior is affected primarily by the fast dynamics. These findings are in agreement with the heterogeneous response interpretation of Chapter 4—the present results showthat, for fluences where

the fast dynamics occur in a large fraction of the sample volume, they dominate the spectroscopic signatures of the slow dynamics, eventually suppressing them.

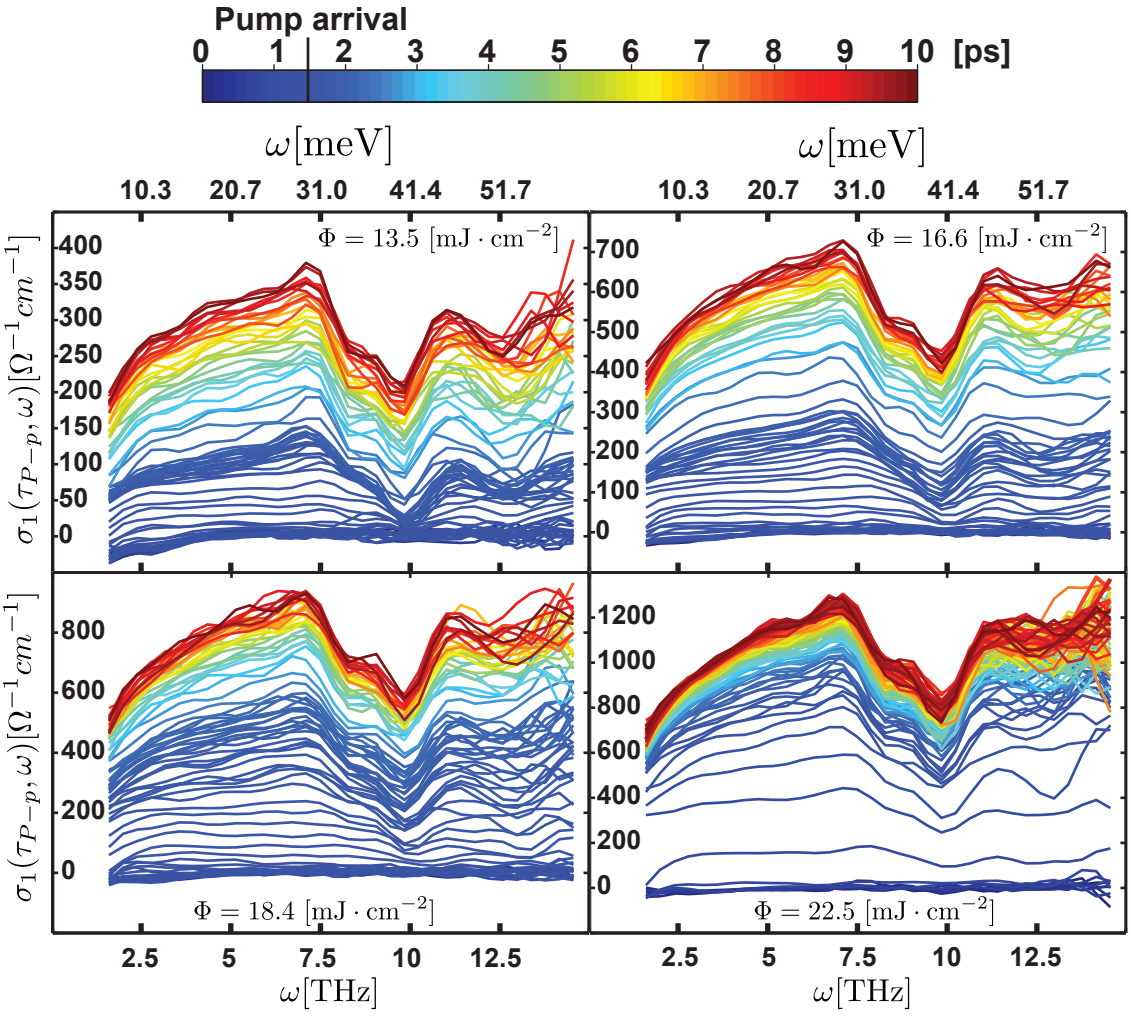

Figure 5–4: Spectrally resolved real conductivity for three characteristic fluences. Each color represents a different pump probe delay as per the color bar. A feature attributed to geometry dependent interference, can clearly be seen between 8 and 10 THz.

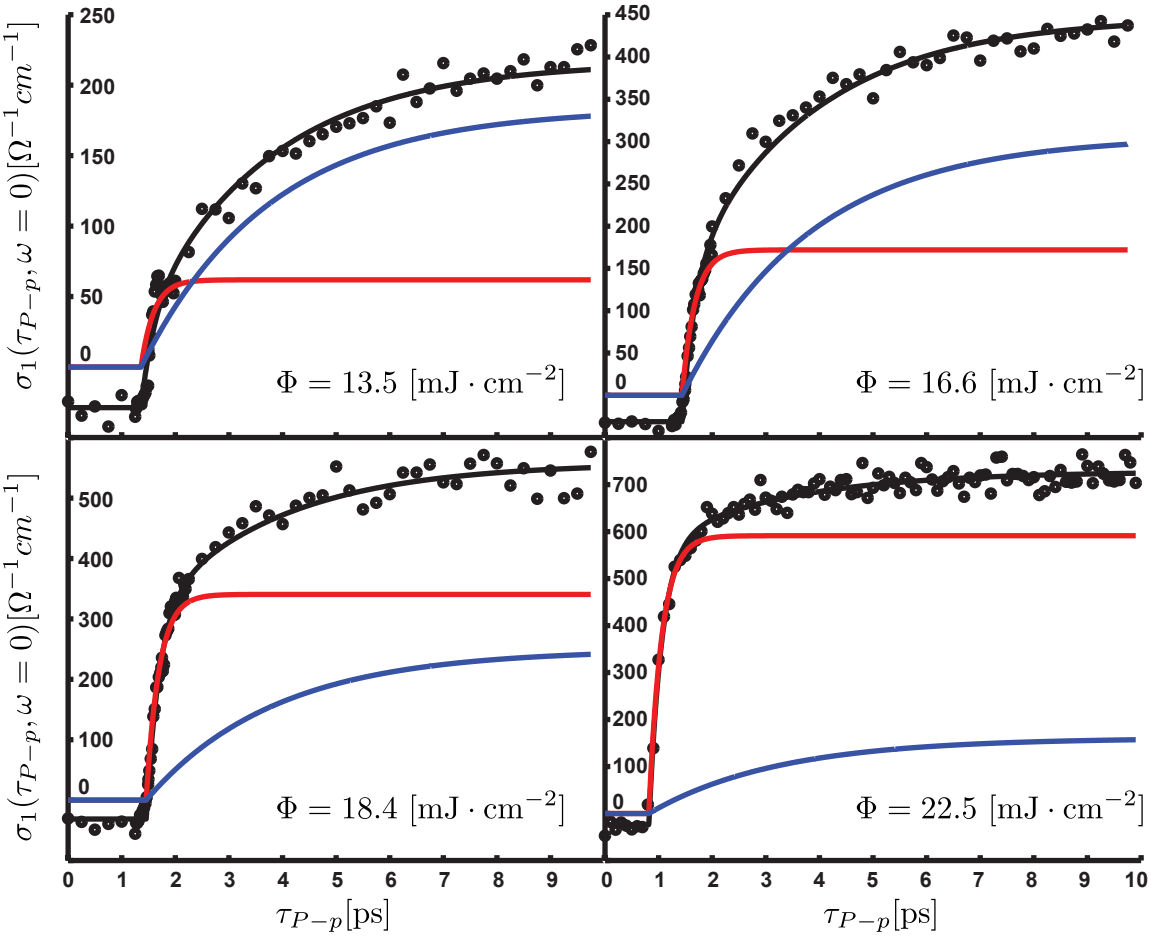

Figure 5–5: Time trace, with biexponential fits, of the extracted direct current conductivity as a function of pump probe time delay for three characteristic fluences. Black markers, the linear extrapolated direct current conductivity for a given pump probe delay; the red, and blue lines are respectively the fast and slow contributions to the dynamics, while the black line is the total biexponential. In grey, the residual of the extracted DC conductivity with the biexponential fit.

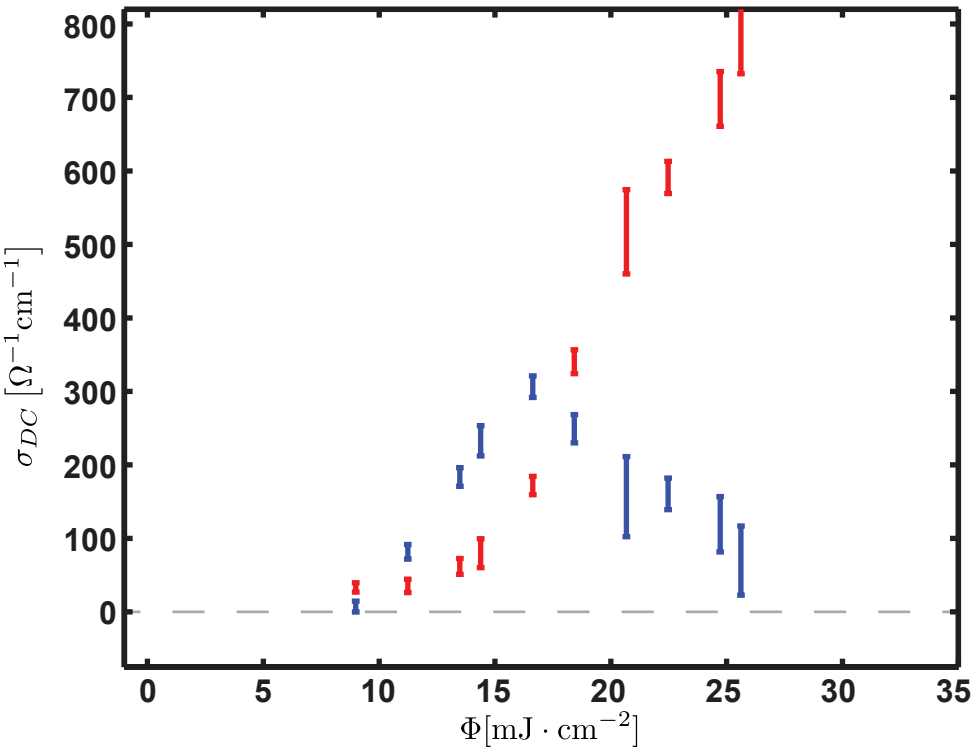

Figure 5–6: Fluence dependence of fast and slow contributions to long time direct current conductivity change. Amplitudes were extracted assuming fast and slow time constants of 240 and 2400 fs respectively. Error bars represent 95% confidence intervals.

5.3 Discussion

5.3.1 $\Phi < \Phi_S$

There is strong evidence for a metastable photoinduced electronic reorganization below the structural phase transition threshold. Our mid infrared results show that there exists a photoinduced phase in this regime for which the band gap is collapsed to below 250 meV. Kubler, Pashkin, *et al.* [46, 47] present data suggesting that the gap collapses to at least 100 meV for these fluences. The terahertz results of this chapter show definitively that the novel metastable phase shown in Chapter 4 and likely measured in [46,47] does not have electronic structure resembling a traditional metal—it is gapped by at least 50 meV.

5.3.2 $\Phi > \Phi_S$

For fluences greater that Φ_S, we have shown that an increasing volume of the sample undergoes a structural phase transition to the tetragonal rutile crystallography of the high temperature phase. Wall *et al.* [43] show that the coherent excitation of the discussed 6 THz modes is maximal at this threshold fluence and is suppressed above it. Our time resolved terahertz measurements show that, above the structural phase transition threshold, VO_2's transient terahertz conductivity approaches metallic character. The dynamics of this transition occur on two distance timescales, one of 240 fs, and one of 2.4 ps. These timescales are consistent with our ultrafast electron diffraction measurement of the structural and astructural phase transitions. That we measure a spectral signature necessarily distinct from the astructural phase transition, but with the same time constant, suggests that a common underlying mechanism is likely able to affect both transitions. For limitingly high fluences, the transient terahertz conductivity of the films approaches the bulk direct current conductivity of equilibrium high temperature VO_2.

5.4 Summary

We have measured, for the first time, the THz regime time resolved spectroscopy of VO_2's photoinduced phase transition. Along with [46, 47] our results show that the metastable M_1 phase reported in Chapter 4 has a significantly, but not entirely, collapsed gap. Above Φ_S, we have shown that the phase transition occurs on a both slow and a fast timescales suggesting the existence of both a thermal and a coherent transition mechanism.

References

[1] E. Dagotto, Science **309**, 257 (2005).

[2] M. Imada, A. Fujimori, and Y. Tokura, Reviews of Modern Physics **70**, 1039 (1998).

[3] P. A. Lee, N. Nagaosa, and X. G. Wen, Reviews of Modern Physics **78**, 17 (2006).

[4] F. J. Morin, Physical Review Letters **3**, 34 (1959).

[5] W. Kaiser et al., *Ultrashort Laser Pulses Generation and Applications*, volume 60 of *Topics in Applied Physics*, Springer-Verlag, Berlin, 1993.

[6] J. R. Dwyer et al., Philosophical Transactions of the Royal Society a-Mathematical Physical and Engineering Sciences **364**, 741 (2006).

[7] M. C. Beard, G. M. Turner, and C. A. Schmuttenmaer, Physical Review B **62**, 15764 (2000).

[8] M. Eichberger et al., Nature **468**, 799 (2010).

[9] H. Ibach and H. Lth, *Solid-state physics : an introduction to principles of materials science*, Advanced texts in physics, Springer, Berlin ; New York, 4th edition, 2009.

[10] B. J. Siwick, J. R. Dwyer, R. E. Jordan, and R. J. D. Miller, Journal of Applied Physics **92**, 1643 (2002).

[11] V. R. Morrison, R. P. Chatelain, C. Godbout, and B. J. Siwick, Opt Express **21**, 21 (2013), 104JF Times Cited:0 Cited References Count:22.

[12] T. van Oudheusden et al., Journal of Applied Physics **102** (2007).

[13] R. P. Chatelain, *Radio-frequencypulsecompression for high-brightness ultrafast electron diffraction: design, characterization and application*, Thesis, 2014.

[14] V. Morrison, *Structural dynamics of the metal-insulator transition in VO_2: an ultrafast electron diffraction study with radio-frequency compressed electron pulses*, Thesis, 2014.

[15] P. U. Jepsen, D. G. Cooke, and M. Koch, Laser & Photonics Reviews **6**, 418 (2012).

[16] D. J. Cook and R. M. Hochstrasser, Optics Letters **25**, 1210 (2000).

[17] M. D. Thomson, M. Kress, T. Loffler, and H. G. Roskos, Laser & Photonics Reviews **1**, 349 (2007).

[18] J. Dai, X. Xie, and X. C. Zhang, Physical Review Letters **97** (2006).

[19] R. A. Kaindl, D. Hagele, M. A. Carnahan, and D. S. Chemla, Physical Review B **79** (2009).

[20] J. B. Goodenough, Journal of Solid State Chemistry **3**, 490 (1971).

[21] J. P. Pouget et al., Journal of Physics and Chemistry of Solids **33**, 1961 (1972).

[22] Villeneu.G et al., Journal of Physics and Chemistry of Solids **33**, 1953 (1972).

[23] P. Lederer, H. Launois, J. P. Pouget, A. Casalot, and Villeneu.G, Journal of Physics and Chemistry of Solids **33**, 1969 (1972).

[24] N. F. Mott and L. Friedman, Philosophical Magazine **30**, 389 (1974).

[25] R. M. Wentzcovitch, W. W. Schulz, and P. B. Allen, Physical Review Letters **72**, 3389 (1994).

[26] R. M. Wentzcovitch, W. W. Schulz, and P. B. Allen, Physical Review Letters **73**, 3043 (1994).

[27] T. M. Rice, H. Launois, and J. P. Pouget, Physical Review Letters **73**, 3042 (1994).

[28] G. Kotliar and D. Vollhardt, Physics Today **57**, 53 (2004).

[29] A. Georges, G. Kotliar, W. Krauth, and M. J. Rozenberg, Reviews of Modern Physics **68**, 13 (1996).

[30] S. Biermann, A. Poteryaev, A. I. Lichtenstein, and A. Georges, Physical Review Letters **94** (2005).

[31] C. Weber et al., Physical Review Letters **108** (2012).

[32] M. W. Haverkort et al., Physical Review Letters **95** (2005).

[33] M. Abbate et al., Physical Review B **43**, 7263 (1991).

[34] T. C. Koethe et al., Physical Review Letters **97** (2006).

[35] M. M. Qazilbash et al., Science **318**, 1750 (2007).

[36] B. Knoll and F. Keilmann, Nature **399**, 134 (1999).

[37] M. M. Qazilbash et al., Physical Review B **83** (2011).

[38] A. Sharoni, J. G. Ramirez, and I. K. Schuller, Physical Review Letters **101** (2008).

[39] M. F. Becker et al., Applied Physics Letters **65**, 1507 (1994).

[40] A. Cavalleri et al., Physical Review Letters **87** (2001).

[41] A. Cavalleri et al., Physical Review B **69** (2004).

[42] A. Cavalleri, T. Dekorsy, H. H. W. Chong, J. C. Kieffer, and R. W. Schoenlein, Physical Review B **70** (2004).

[43] S. Wall et al., Nature Communications **3** (2012).

[44] P. Baum, D. S. Yang, and A. H. Zewail, Science **318**, 788 (2007).

[45] D. J. Hilton et al., Physical Review Letters **99** (2007).

[46] C. Kubler et al., Physical Review Letters **99** (2007).

[47] A. Pashkin et al., Physical Review B **83** (2011).

[48] M. M. Qazilbash et al., Physical Review B **74** (2006).

[49] V. Morrison et al., submitted to Science (2014), arXiv:1407.1304.

[50] A. Hendaoui, N. Emond, S. Dorval, M. Chaker, and E. Haddad, Current Applied Physics **13**, 875 (2013).

[51] B. Fultz and J. M. Howe, *Transmission electron microscopy and diffractometry of materials*, Physics and astronomy online library, Springer, Berlin ; New York, 2nd edition, 2002.

[52] B. J. Siwick, J. R. Dwyer, R. E. Jordan, and R. J. Miller, Science **302**, 1382 (2003).

[53] J. C. Zheng, Y. M. Zhu, L. J. Wu, and J. W. Davenport, Journal of Applied Crystallography **38**, 648 (2005).

[54] J. M. Zuo, Reports on Progress in Physics **67**, 2053 (2004).